UCLA
UCLA Previously Published Works

Title

Polar and mid-latitude vortices and zonal flows on Jupiter and Saturn

Permalink

https://escholarship.org/uc/item/3m22m0rx

Authors

Heimpel, Moritz H
Yadav, Rakesh K
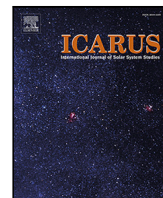Featherstone, Nicholas A
et al.

Publication Date

2022-06-01

DOI

10.1016/j.icarus.2022.114942

Peer reviewed

Research Paper

Polar and mid-latitude vortices and zonal flows on Jupiter and Saturn

Moritz H. Heimpel [a],[*], Rakesh K. Yadav [b], Nicholas A. Featherstone [c], Jonathan M. Aurnou [d]

[a] University of Alberta, Department of Physics, Edmonton, Alberta, T6G 2E1, Canada
[b] Department of Earth and Planetary Sciences, Harvard University, Cambridge, MA 02138, USA
[c] Southwest Research Institute, 1050 Walnut Street, Suite 426, Boulder, CO 80302, USA
[d] Department of Earth, Planetary, and Space Sciences, University of California, Los Angeles, CA 90095, USA

ARTICLE INFO

ABSTRACT

Zonal flow on Jupiter and Saturn consists of equatorial super-rotation and alternating East–West jet streams at higher latitudes. Interacting with these zonal flows, numerous vortices occur with various sizes and lifetimes. The Juno mission and Cassini's grand finale have shown that the zonal jets of Jupiter and Saturn extend deeply into their molecular envelopes. On Jupiter, the vast majority of low and mid-latitude jovian vortices are anticyclonic, whereas cyclones appear at polar latitudes. Cassini mission observations revealed a similar pattern on Saturn; its North and South polar vortices are cyclonic, whereas anticyclones occur at mid-latitudes. We use the recently developed code *Rayleigh* to run high-resolution simulations of rotating convection in 3D spherical shells. Four models are presented that result in dynamical flows that are comparable to those on the giant planets. We confirm previous results, finding that deep convective turbulence can explain the structure of jets. However, the latitude and the strength and depth of stable stratification can modify jet morphologies and affect the formation and dynamics of vortices. Lower latitudes favour shallow anticyclonic vortices that form due to upward and divergent flow near the outer boundary. These anticyclones are typically shielded by cyclonic filaments associated with downwelling return flow. In contrast, a single polar cyclone, or clusters of cyclones form near the poles. All of our simulations have this global pattern; a strong preference for shallow anticyclones in the first anticyclonic shear zone away from the equatorial jet (corresponding to the region of the Great Red Spot on Jupiter and Storm Alley on Saturn), cyclonic and anticyclonic vortices at higher mid-latitudes, and a deeply seated cyclone or cyclone clusters at each pole. Our results show that Juno and Cassini observations of cloud-level flow can be explained in terms of deep convective dynamics in the molecular envelopes of Jupiter and Saturn.

1. Introduction

The gas giants Jupiter and Saturn are composed mostly of fluid Hydrogen with minor amounts of Helium and traces of other elements. Electrical conductivity is dynamically negligible in much of the molecular envelope. However, the conductivity increases by several orders of magnitude as molecular Hydrogen dissociates progressively to a depth where a metallic state is reached. The depth of transition to a metallic fluid has been estimated for Jupiter (roughly 80%–90% of Jupiter's radius) and Saturn (60%–75% of Saturn's radius) based on laboratory experiments (Nellis et al., 1999), ab-initio computational models (French et al., 2012), and from inversions of magnetic field data from the Cassini (Dougherty et al., 2018) and Juno (Moore et al., 2018) missions. Precipitation of Helium in both planets is expected to affect heat flow and buoyant stability, which can result in stable stratification near the bottom of the molecular envelope and in the metallic interiors of Jupiter and Saturn (Stevenson and Salpeter, 1977b,a; Militzer

et al., 2016; Wahl et al., 2017). Recent numerical models have shown that a stable layer promotes multiple jets (Gastine and Wicht, 2021; Christensen et al., 2020).

The global magnetic fields of Jupiter and Saturn are sustained by the dynamo process, which is driven by convection. At great depths, and in the transition region of the lower molecular envelope, magnetic Lorentz forces limit flow velocities. Theoretical considerations indicate that maximum flow velocities in the dynamo regions of Jupiter and Saturn are much lower than the order 100 m/s velocities of cloud level zonal flows. Estimates of convective velocities in the dynamo regions of giant planets range between roughly 1 mm/s (Cao and Stevenson, 2017) and 1 m/s (Starchenko and Jones, 2002). Deep convection dynamo models with variable radial electrical conductivity have shown that zonal flows are weak in the dynamo regions (Heimpel and Gómeza Pérez, 2011; Gastine et al., 2014b). Scaling studies of numerous anelastic dynamo

---

* Corresponding author.
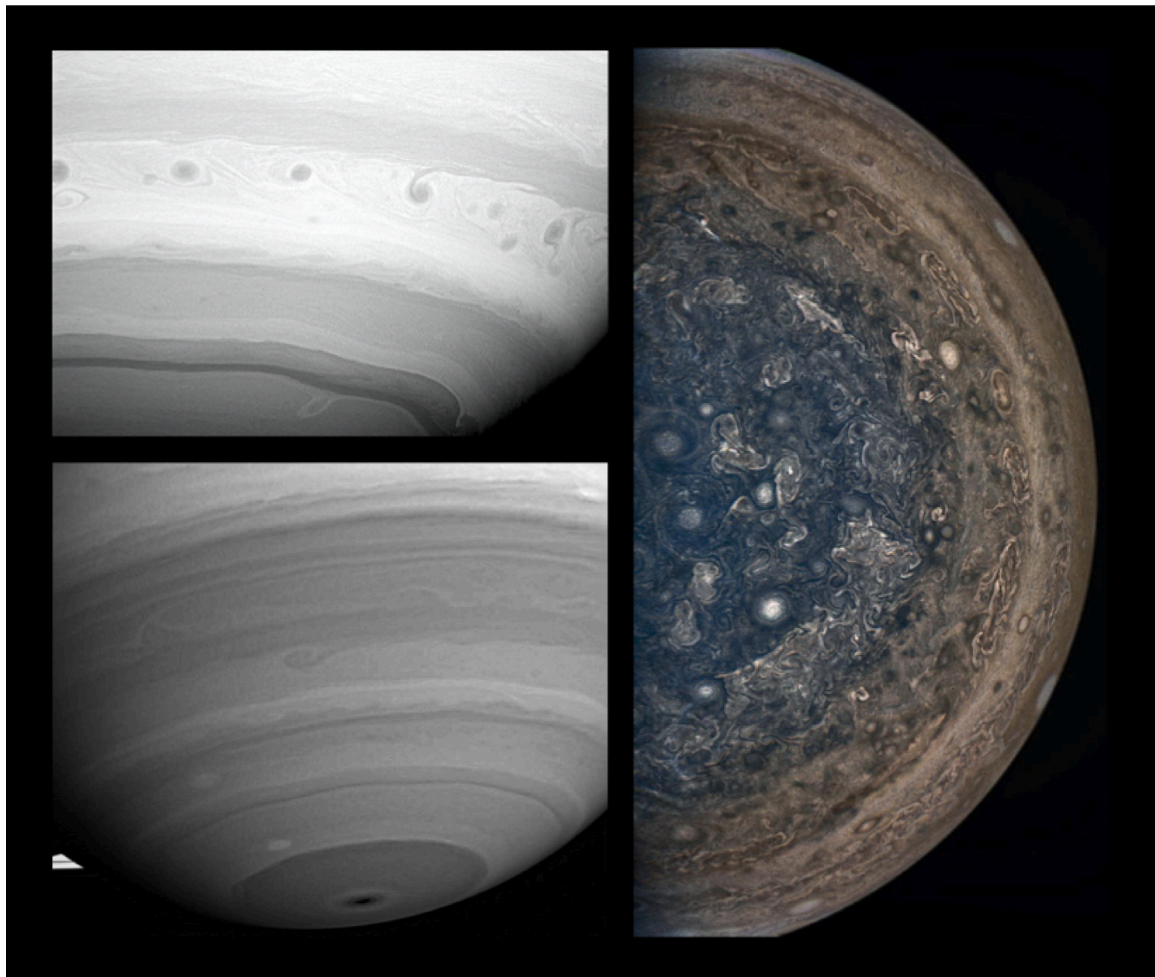 *E-mail address:* mheimpel@ualberta.ca (M.H. Heimpel).

Fig. 1. Top left: NASA Cassini 2008 image PIA10411 of Saturn's southern mid-latitudes shows anticyclones in the anticyclonic shear band near the equatorial jet. Bottom left NASA Cassini 2005 PIA07585 image shows the south polar cyclone. Right: NASA Juno 2017 PIA21382 image shows several cyclonic vortices near Jupiter's south pole.
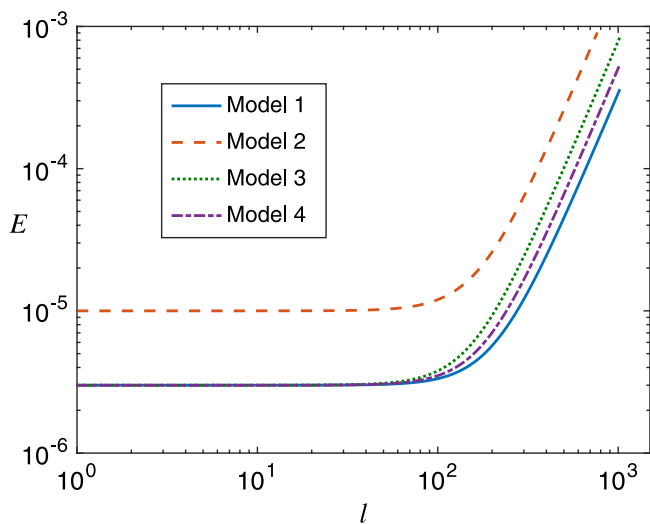

Fig. 2. Hyperdiffusion models shown as Ekman number $E(l) = \epsilon(l)Ek$ as a function of spherical harmonic degree l for the four simulations.

Fig. 3. Conductive entropy gradient ds_c/dr for the four simulations (Note the inverted vertical axis). The shape of each forcing function is controlled by the equation of state and boundary conditions (constant ds_c/dr at the inner and outer boundaries). The grey dashed lines indicate $ds_c/dr = -1$ (convective inner boundary condition) and $ds_c/dr = 0$ (neutral stratification). For Model 1, the inner boundary is at $r = r_i = 0.90$. For Models 2, 3 and 4 the inner boundary is at $r = 0.95$. For all models the entropy gradient is stably stratified at the outer boundary ($ds_c/dr > 0$ at $r = r_o = 1$).

models confirm the characteristic truncation of zonal flows in the dynamo region and yield convective velocity estimates of roughly 1–3 cm/s when applied to Jupiter (Yadav et al., 2013; Duarte et al.,
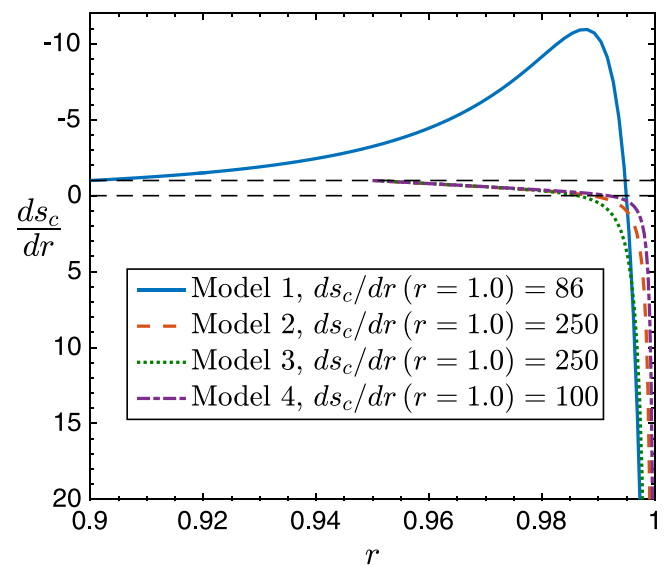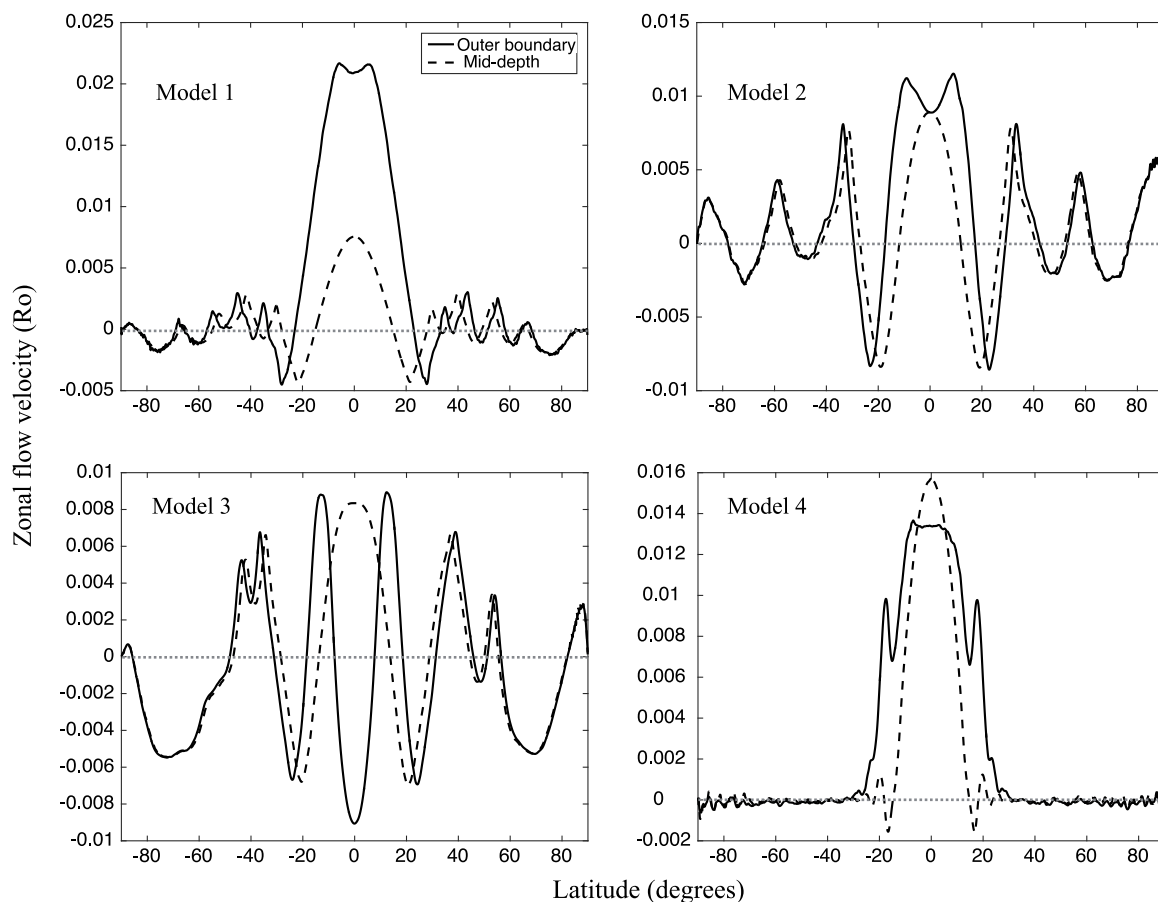
Fig. 4. Zonal flow velocity for the four models. Velocities are scaled as the planetary Rossby number, $Ro = V_\phi/(\Omega r_o)$, where V_ϕ is the axisymmetric azimuthal velocity (zonal velocity).

2018). Maximum depths of fast zonal flow (of order 10 m/s) have been estimated to correspond to $0.96\,R_J$ and $0.86\,R_S$, where R_J and R_S are radii at the cloud level of Jupiter and Saturn, respectively (Liu et al., 2008; Heimpel and Gómeza Pérez, 2011).

Recent observational results from the Juno mission to Jupiter and the Cassini Grand Finale Saturn observations indicate that zonal jets extend deeply within the molecular envelopes of both planets (Kaspi et al., 2018; Guillot et al., 2018; Galanti et al., 2019; Duer et al., 2021). Although it is not fully understood how high latitude atmospheric jets couple to the metallic interior fluid, computational models have shown that flow in the dynamo region is slow, whereas convection extending outward into the semiconducting molecular envelope can drive fast equatorial zonal flows (Heimpel and Gómeza Pérez, 2011; Jones, 2014; Gastine et al., 2014b; Wicht and Gastine, 2020).

Comparing the atmospheric dynamical features of Jupiter and Saturn, particularly the zonal jets and vortices, the similarities and differences are equally compelling. Each planet has a dominant prograde equatorial jet and several high latitude jets. Saturn's jets are broader and faster than those of Jupiter. However, the Rossby number based on a length scale equal to the depth of the molecular envelope is roughly similar for Jupiter and Saturn. Saturn's jets are relatively symmetrical about the equator, whereas significant North–South asymmetry is observed for Jupiter (Vasavada and Showman, 2005).

There have been numerous observations consistent with a preference for anticyclones over cyclones for the mid-latitudes of the gas giants, including Jupiter's Great Red Spot (GRS) and White Ovals, and Saturn's great storm of 2010–2011 (Sayanagi et al., 2013; Vasavada and Showman, 2005). Although the mid-latitude anticyclone preference is more clear for Jupiter than for Saturn, each planet has a highly active region that hosts anticyclones at latitudes corresponding to the first

anticyclonic shear zone away from the equator. For Saturn this zone has been referred to as Storm Alley (Vasavada et al., 2006). However, both planets have cyclonic vortices at the poles. Saturn has a single cyclone at each pole, while Jupiter has clusters of several circumpolar cyclones (CPC) in the North and South polar regions (Adriani et al., 2018; Grassi et al., 2018; Brueshaber et al., 2019; Cai et al., 2021; Siegelman et al., 2022). The tendency for vortices at the poles to be cyclonic has been explained as a result of the global radial vorticity gradient, which can cause cyclonic vortices to drift poleward (the beta-drift mechanism) (Li et al., 2020; O'Neill et al., 2015). Fig. 1 shows images of anticyclones in Saturn's Storm Alley, the southern polar cyclone, and several CPC in Jupiter's south polar region.

Deeply seated polar vortices have been modelled in recent nonmagnetic deep convection models using the Boussinesq (Garcia et al., 2020) and anelastic (Yadav and Bloxham, 2020) approximations. However, recent dynamo models have shown that magnetic coupling in the transition region from the molecular envelope to the dynamo interior can affect the formation and scale of vortices (Yadav et al., 2020). The anelastic deep convection models of Heimpel et al. (2015) focused on the formation of relatively shallow anticyclonic vortices that can occur at all latitudes but are more numerous at mid-latitudes near the equatorial jet.

As in previous non-magnetic rotating convection models, we restrict our attention to the molecular envelope (Garcia et al., 2020; Yadav and Bloxham, 2020; Heimpel et al., 2015; Gastine et al., 2014a; Jones and Kuzanyan, 2009; Kaspi et al., 2009; Heimpel et al., 2005), and choose inner boundary radii representative of the transition from fast to slow zonal flow, in the region of the molecular layer of Jupiter, outside the region strongly affected by Lorentz forces. We present one model with $r_i = 0.9\,r_o$, and three models with $r_i = 0.95\,r_o$, where r_i
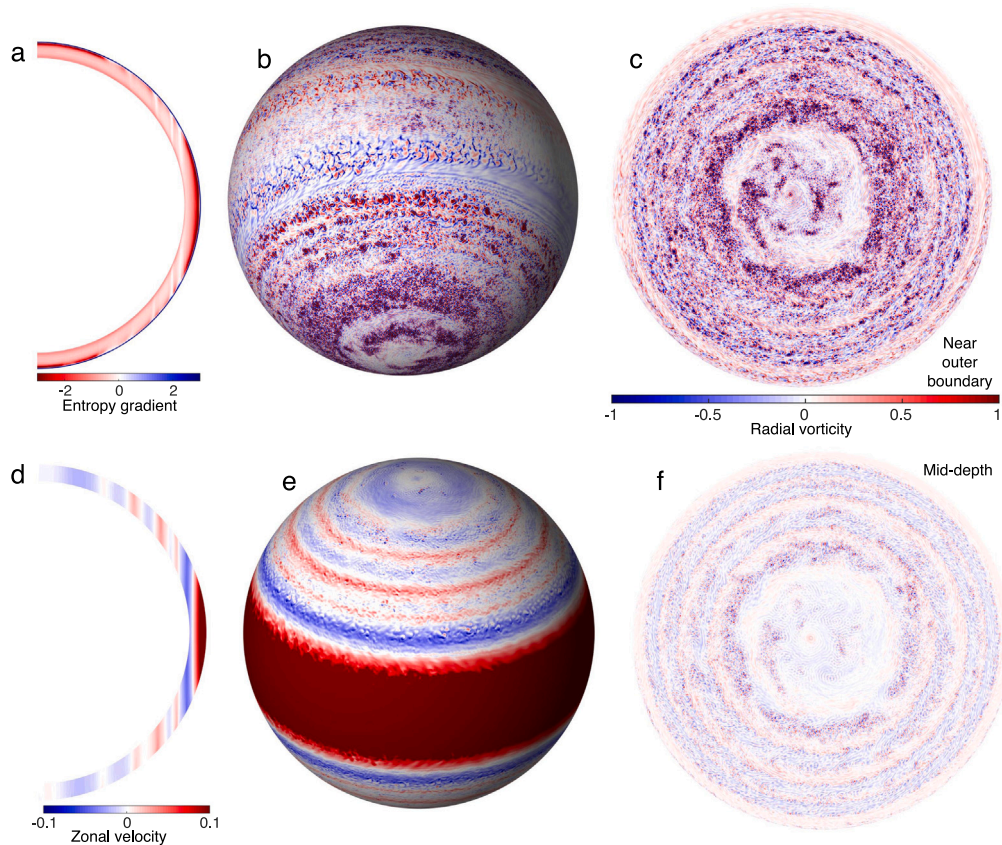
Fig. 5. Images of fluid flow and entropy gradient at a snapshot in time, near the end of Model 1. **a**, Azimuthally averaged radial entropy gradient. Blue indicates stable stratification, red deeper convection. **b**, Perspective south polar view (camera at $-30°$ latitude) of radial vorticity near the outer boundary. Cyclonic (anticyclonic) vorticity is red (blue) in the northern hemisphere, and blue (red) in the southern hemisphere. Vorticity is scaled by the background rotation rate Ω. **c**, North polar view (camera at $90°$ latitude) of radial vorticity near the outer boundary. **d**, Azimuthally averaged azimuthal (zonal) velocity in Rossby number units based on the shell depth. **e**, Perspective north polar view (camera at $30°$ latitude) of azimuthal (zonal) velocity near outer boundary. (Colour bar is shared between d and e). **f**, North polar view of radial vorticity near at mid-shell depth. (Colour bar is shared between b, c and f). Note: the scaling of velocity colour bar is in Rossby number based on shell depth $Ro_d = v/(\Omega d)$. (For interpretation of the references to colour in this figure legend, the reader is referred to the web version of this article.)

and r_o are the inner and outer boundary radii, respectively. In addition we assume stable stratification of the shallow atmosphere, consistent with the results of the Galileo probe (Magalhães et al., 2002). The transition between Jupiter's convective interior and its stably stratified atmosphere is modelled by applying uniform superadiabatic (convective) entropy flux at the inner boundary of the spherical shell, and uniform subadiabatic (stabilizing) flux at the outer boundary (Heimpel et al., 2015).

2. Methods

2.1. Computational code and numerical simulations

The numerical dynamo code *Rayleigh* solves the governing equations of magnetohydrodynamics in spherical geometry under the anelastic approximation (Featherstone and Hindman, 2016; Matsui et al., 2016). We ran *Rayleigh* in non-magnetic, rotating convection mode. MPI parallelization of *Rayleigh* is done in two dimensions. This parallelization allowed us to run large-scale models, utilizing up to 524,288 cores for our largest simulation on the recently retired massively parallel IBM Blue Gene supercomputer *Mira*, a 10-petaflops IBM Blue Gene/Q system at Argonne National Laboratory. Data from the models described here are available through the Rayleigh Simulation Library (Featherstone et al., 2021), which is hosted at the University of Colorado and is publicly accessible through a Globus endpoint. This library was developed by the Rayleigh user community and hosts geodynamo, planetary dynamo, and stellar dynamo data sets.

2.2. Governing equations

Consider a compressible fluid in a spherical shell rotating at a constant rotation rate Ω about the z-axis. The anelastic approximation allows for the incorporation of density stratification while filtering out fast acoustic waves. In our anelastic formulation entropy serves as the single fluctuating thermodynamic variable (Lantz and Fan, 1999; Gastine and Wicht, 2012). We adopt a dimensionless formulation using Ω^{-1} as the time unit, and the shell thickness $d = r_o - r_i$ as the reference length scale. Density, temperature and gravity are non-dimensionalized using their values at the outer boundary r_o. The hydrostatic and adiabatic reference state is given by $d\tilde{T}(r)/dr = -Di\,g$, where Di is the dissipation number

$$Di = \frac{g_o d}{c_p T_o} \tag{1}$$

and where g_o and T_o are the reference gravity and temperature at the outer boundary, respectively. Assuming an ideal gas leads to a polytropic equation of state given by $\tilde{\rho}(r) = \tilde{T}(r)^n$; we use polytropic indices $n = 1$ and $n = 2$ here. A polytropic index $n = 1$ gives a linear increase of density with depth, and has been used as a good approximation for the Jovian molecular envelope (Hubbard, 1999), whereas $n = 2$ was used in more recent numerical models and gives a better approximation for the density–temperature dependence (Jones et al., 2009; Jones and Kuzanyan, 2009; Gastine and Wicht, 2012). We assume that the mass is concentrated in the inner part, such that $g \propto 1/r^2$ provides a good first-order approximation of the gravity profile in the molecular envelope of a giant planet (Jones and Kuzanyan,
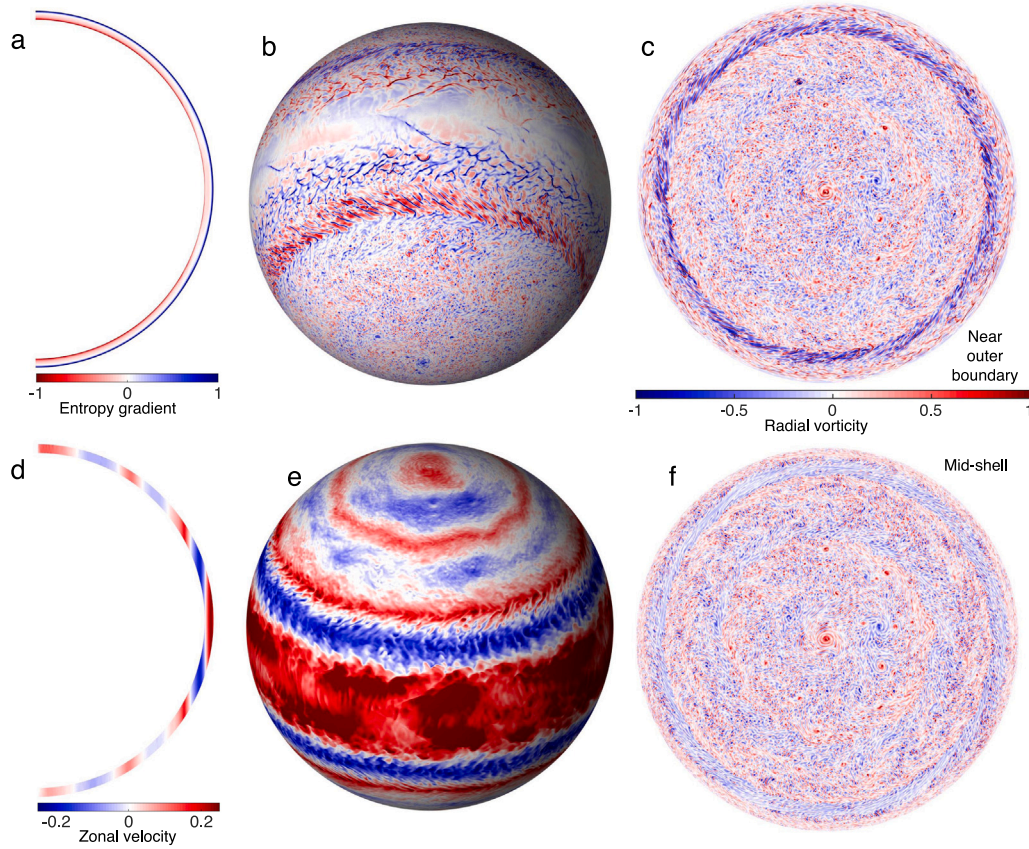
Fig. 6. Images of fluid flow and entropy gradient at a snapshot in time, near the end of Model 2. See Fig. 5 for image descriptions. (For interpretation of the references to colour in this figure legend, the reader is referred to the web version of this article.)

2009; Gastine and Wicht, 2012). This leads to the following background temperature $\tilde{T}(r)$ and density $\tilde{\rho}(r)$ profiles

$$\tilde{T}(r) = \frac{Di}{(1-\eta)^2 r} + 1 - \frac{Di}{1-\eta}, \quad \tilde{\rho}(r) = \tilde{T}(r)^n \quad \text{and} \quad Di = \eta \left(\exp \frac{N_\rho}{n} - 1 \right),$$
(2)

where $N_\rho = \ln \tilde{\rho}(r_i)/\tilde{\rho}(r_o)$ is the number of density scale heights of the background density profile $\tilde{\rho}(r)$, and $\eta = r_i/r_o$ is the radius ratio of the spherical shell (Gastine and Wicht, 2012).

The equations that govern compressible convection under the anelastic approximation are given by

$$\nabla \cdot \left[\tilde{\rho}(r)\boldsymbol{v} \right] = 0,$$
(3)

$$\frac{\partial \boldsymbol{v}}{\partial t} + \boldsymbol{v} \cdot \nabla \boldsymbol{v} + 2\boldsymbol{e_z} \times \boldsymbol{v} = -\nabla \frac{p}{\tilde{\rho}(r)} + Ra^* \frac{r_o^2}{r^2} s \, \boldsymbol{e_r} + \frac{Ek}{\tilde{\rho}(r)} \nabla \cdot D,$$
(4)

$$\tilde{\rho}(r)\tilde{T}(r) \left(\frac{\partial s}{\partial t} + \boldsymbol{v} \cdot \nabla s \right) = \frac{Ek}{Pr} \nabla \cdot \left[\tilde{\rho}(r)\tilde{T}(r)\nabla s \right] + Q(r) + \frac{Ek \, Di}{Ra^*} \, \Phi,$$
(5)

where $\boldsymbol{v}$, p and s are velocity, pressure, and entropy, respectively, and $Q(r)$ is an entropy source or sink. The components of the traceless rate-of-strain tensor D are given by

$$D_{ij} = 2\tilde{\rho}(r) \left(\mathrm{e}_{ij} - \frac{1}{3}\delta_{ij}\nabla \cdot \boldsymbol{v} \right) \quad \text{with} \quad \mathrm{e}_{ij} = \frac{1}{2} \left(\frac{\partial v_i}{\partial x_j} + \frac{\partial v_j}{\partial x_i} \right),$$
(6)

where δ_{ij} are the components of the identity matrix, and $\Phi(r, \theta, \phi)$ is the viscous heating contribution expressed by

$$\Phi = 2\tilde{\rho}(r) \left[\mathrm{e}_{ij}\mathrm{e}_{ji} - \frac{1}{3}(\nabla \cdot \boldsymbol{v})^2 \right].$$
(7)

The conductive entropy profile $s_c(r)$ is obtained from the entropy equation by solving the thermal equilibrium equation:

$$\nabla \cdot \left[\tilde{\rho}(r)\tilde{T}(r)\nabla s \right] = -\frac{Pr}{Ek}Q(r)$$
(8)

with the chosen boundary conditions. The value of the volumetric entropy sink $Q(r)$, is set to balance the entropy flux boundary conditions such that thermal energy conservation is ensured.

The system of Eqs. (3)–(5) is controlled by three non-dimensional numbers: the Ekman number $Ek = \nu/\Omega d^2$; the Prandtl number $Pr = \nu/\kappa$ and the Rayleigh number $Ra^* = -g_o\beta_i/c_p\Omega^2$, where β_i is the entropy gradient ds_c/dr at r_i, the inner boundary radius. We use constant entropy flux and free-slip velocity boundary conditions at the top spherical shell boundary r_o. Free-slip or no-slip boundary conditions are used at the bottom boundary r_i. Convection is driven by the imposed negative entropy gradient at the inner boundary, and suppressed by the positive gradient at the outer boundary. These entropy gradient boundary conditions perturb the adiabatic background state. Through the volume of the spherical shell, convection and stability are forced by the conductive entropy gradient ds_c/dr. Where ds_c/dr is negative, the forcing is convective (superadiabatic). Stably stratified (subadiabatic) forcing occurs where ds_c/dr is positive.

Resolution constraints in 3D spherical numerical rotating convection and dynamo models require viscosity (and the Ekman number) to be orders of magnitude higher than those estimated for Jupiter and Saturn (e.g. Duarte et al. (2018) and Yadav et al. (2013)). However, we use high resolution grids (See Table 1) compared to previous models. The highest resolution models have 1024 radial levels (Model 4) and 0.12 degree latitudinal resolution with maximum spherical harmonic degree $l_{max} = 1023$ (Models 1, 3 and 4). Nevertheless, given our relatively small Ekman numbers and large Rayleigh numbers, the convergence of these numerical models still requires the use of hyperdiffusivity. Thus, the
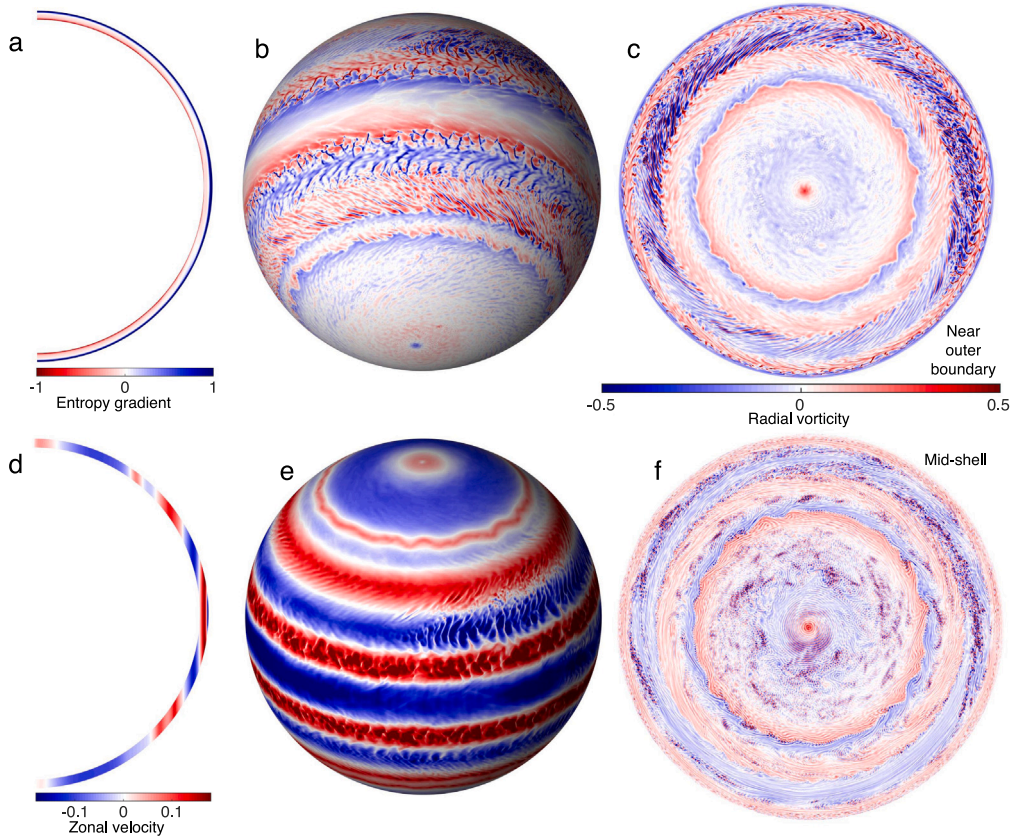
Fig. 7. Images of fluid flow and entropy gradient at a snapshot in time, near the end of Model 3. See Fig. 5 for image descriptions. (For interpretation of the references to colour in this figure legend, the reader is referred to the web version of this article.)

diffusive terms entering in Eqs. (4)–(5) are multiplied by an operator of the functional form

$$\epsilon(\ell) = \left(1 + \alpha \left[\frac{\ell - 1}{\ell_{\max} - 1} \right]^{\beta} \right). \tag{9}$$

Here, $\epsilon(\ell)$ is the hyperdiffusivity function (Kuang and Bloxham, 1999), which depends on the spherical harmonic degree ℓ, the maximum spherical harmonic degree $\ell_{\max}$, the hyperdiffusion amplitude α, and the hyperdiffusion exponent $\beta = 3$. Fig. 2 shows the final hyperdiffusivity functions in terms of the harmonic degree dependent Ekman number $E(l) = \epsilon(l)Ek$ used for the four models (see also Eq. (9) and Table 1). For given values of Ra and Ek the amplitudes of hyperdiffusion have been reduced stepwise as the simulations approached a statistically steady-state. Hyperdiffusion was changed upon restarting a model. Each change in hyperdiffusion resulted in a transient perturbation of the kinetic energy, which was allowed to settle to a state where the mean energy remained relatively constant.

Hyperdiffusion can potentially introduce anisotropy between the horizontal and the radial directions as $\epsilon(\ell)$ depends on the horizontal scale only, and it yields artificial viscous heating that can affect the heat transport balance. However, in test runs at higher Ek than those presented here, we have compared results with and without hyperdiffusion. We found that the large scale features (e.g. jet streams) are not strongly affected by hyperdiffusion. Vortices, however, can be more strongly affected, depending on the level of hyperdiffusion. In particular smaller scale flow structures such as cyclonic filaments can be blurred. For the models presented here hyperdiffusion becomes significant at spherical harmonic degree $\ell \sim 100$ (Fig. 2). Thus, although we estimate that jets and the scale of whole vortices are not strongly affected, the cyclonic filaments would be finer (and require greater resolution) without hyperdiffusion.

Table 1

List of numerical simulations. The number of latitudinal grid points $n_\theta = n_\phi/2 = 3(l_{max}+1)/2$, where n_ϕ is the number of longitudinal grid points and l_{max} is the maximum number spherical harmonic degrees. Neutral Stability Radius (NSR) is the radius at which the conductive entropy gradient $ds_c/dr = 0$ (see Fig. 3). Internal heating types for *Rayleigh*. The number 4 corresponds to constant heat sink (10), 1 corresponds to radially variable cooling (11). For all runs the top mechanical boundary conditions are free-slip. The bottom boundary conditions listed are either free-slip (FS) or no-slip (NS).

Parameter or Condition	Model 1	Model 2	Model 3	Model 4
Ek	3×10^{-6}	1×10^{-5}	3×10^{-6}	3×10^{-6}
Ra^*	0.048	0.75	0.6	10.0
Pr	1	0.3	1	1
r_i/r_o	0.9	0.95	0.95	0.95
n_r	256	384	512	1024
n_θ	1536	1152	1536	1536
n	2.0	1.0	2.0	1.0
N_ρ	5.0	5.0	7.0	5.0
NSR	0.995	0.989	0.987	0.992
α	120	90	280	180
Run time (Ω^{-1})	3.81×10^3	1.91×10^3	1.87×10^4	4.75×10^3
Heating type	4	1	1	1
Bottom B.C.	FS	FS	FS	NS

Given the intensive computational requirements needed for this study, and the limited resources available, we chose to perform a limited number of very high resolution models. Each model run was initiated at moderate values of the input parameters. Checkpoint output files were then saved, and runs were restarted with new parameters requiring higher resolution. For example, the initial runs that led to Model 4 were started with most parameters the same as Model 4. We explored models with different Ra^* and heating conditions. The production runs presented here were all started at lower resolution and
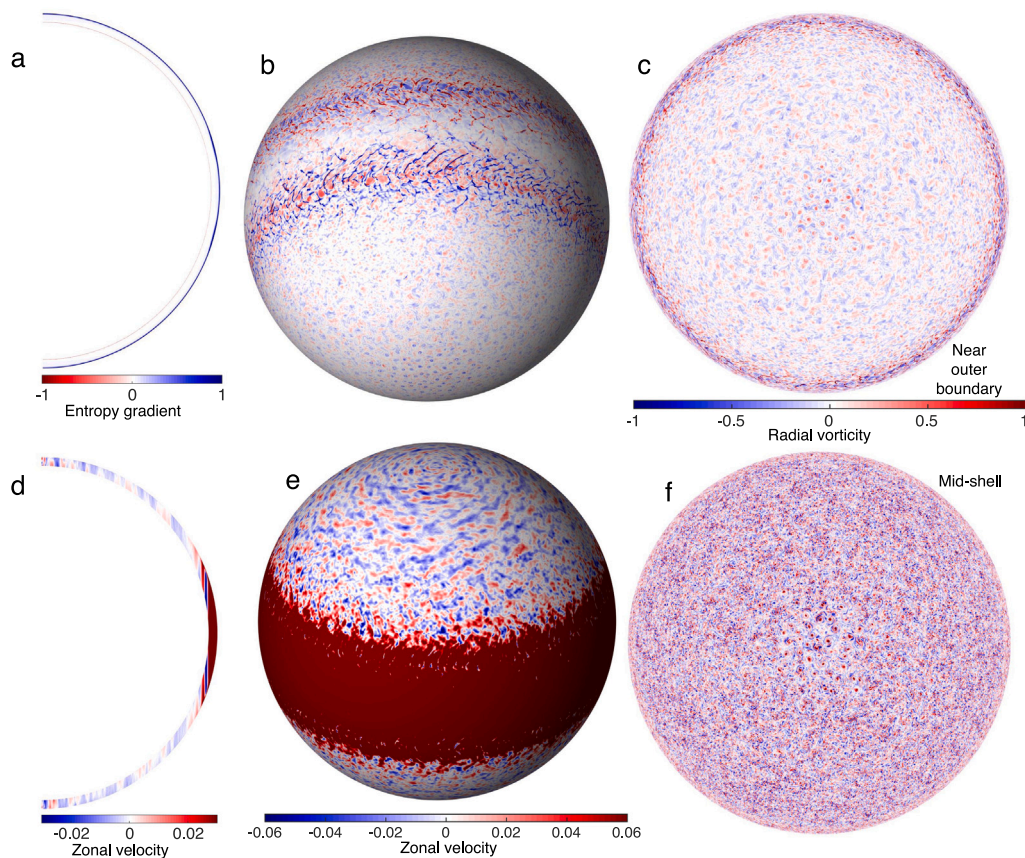
Fig. 8. Images of fluid flow and entropy gradient at a snapshot in time, near the end of Model 4. See Fig. 5 for image descriptions. In this figure the colour bars differ between d and e. (For interpretation of the references to colour in this figure legend, the reader is referred to the web version of this article.)

with higher Ekman number (typically $Ek = 10^{-4}$). Subsequent runs were then restarted with decreasing Ek, requiring increased resolution. Our goal in presenting these results is not a definitive parameter study. Instead we present the variation in dynamics for a small number of high resolution simulations with a range of velocity boundary conditions and heating conditions. This presentation of models can provide some insight into the effect of these conditions on the development on jets and vortices on the giant planets.

3. Model setup

We present four model simulations. Table 1 shows parameters and conditions for the four models. Model 1 has the same parameters as a previous model (Heimpel et al., 2015). However, in that previous work a four-fold longitudinal symmetry condition was used due to the constraints on computational resources. That four-fold symmetry condition did not allow a realistic analysis of polar vortex features. Here, all four models are computed in a full sphere with no longitudinal symmetry conditions. We find that the zonal flow and vortices are broadly similar for Model 1 as compared to the model from Heimpel et al. (2015). For three of the four models, including Model 1, we do observe single dominant polar cyclones in each hemisphere, which we detail below, in Sections 4.2 and 4.3. All four models have convective bottom heat flux $(ds_c/dr < 0)$ and stable top heat flux $(ds_c/dr > 0)$ boundary conditions. Models 1, 2 and 3 have top and bottom free-slip (FS) velocity boundary conditions. Model 4 has mixed velocity boundary conditions, with FS at the top $(r = r_o)$ and no-slip (NS) at the bottom $(r = r_i)$.

A volumetric heat sink is required in these models to balance the imposed boundary entropy gradient. Two different heating types are

used. Fig. 3 shows the heating profiles for the four models. For Model 1 we implement a uniform heat sink (internal cooling)

$$Q = \gamma. \tag{10}$$

This heating type was used in Heimpel et al. (2015) and provides forcing that is variable in radius and inversely proportional to $\tilde{\rho}(r)\tilde{T}(r)$. For subadiabatic heat flux boundary conditions at the outer boundary this heating type can result in a peak in the convective forcing at shallow depth, with decreasing convective forcing at greater depths (See Table 1 and Fig. 3). For Models 2, 3 and 4 the heating profile is

$$Q(r) = \gamma \tilde{\rho}(r)\tilde{T}(r). \tag{11}$$

This profile assumes turbulent entropy diffusion and specific entropy decreases that are uniform in space over time. It has been used in models of Jupiter's dynamo (Jones, 2014). As with the uniform internal cooling, this radially variable condition provides increasing convective forcing with depth. However, the two cooling conditions differ in their depth dependence (See Table 1 and Fig. 3). Although all of our models include a stratified outer layer, they do not simulate atmospheric processes that can be important for a weather layer, such as cloud physics and moist convection (Ingersoll et al., 2004).

The heating profiles (i.e. conductive entropy gradient profiles ds_c/dr) for the four models are plotted in Fig. 3. The difference between the constant internal cooling (Model 1) and radially variable cooling (Models 2, 3 and 4) is apparent. For Model 1, convective forcing is relatively shallow – neutral buoyancy $(ds_c/dr = 0)$ occurs at $r \simeq 0.995$ and convective forcing peaks at $r \simeq 0.987$. Also apparent is the difference that different choices of the polytropic index have on thermal forcing (See Table 1). Models 2 and 3 have polytropic indices $n = 1$ and $n = 2$, respectively, with the same entropy gradient boundary condition
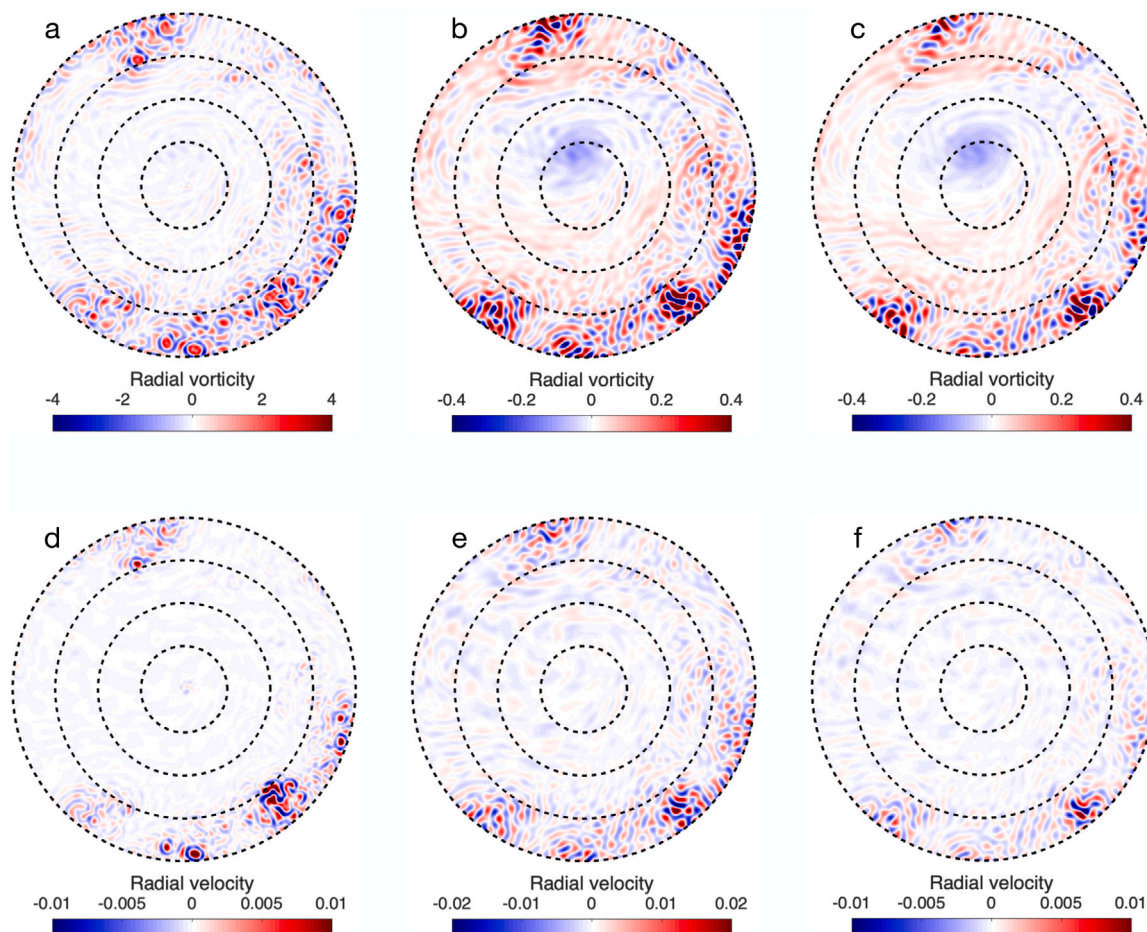
Fig. 9. Zoomed-in south polar view of radial vorticity (**a, b, c**) and radial velocity (**d, e, f**) at three different depths for Model 1 (compare to Fig. 5). The depths correspond to $r = 0.9991r_o$ (**a, d**), $r = 0.9503r_o$ (**b, e**) and $r = 0.9149r_o$ (**c, f**), with $r_i = 0.9r_o$. Dashed contours show latitudes of $-78°$, $-81°$, $-84°$, $-87°$. Because these images show the southern hemisphere cyclonic (anticyclonic) vorticity corresponds to blue (red) colours. (For interpretation of the references to colour in this figure legend, the reader is referred to the web version of this article.)

at the outer boundary ($ds/dr = 250$). This difference in polytropic index results in a deeper stably stratified layer for Model 3.

4. Model results

4.1. Zonal flow

Fig. 4 shows the zonal flow profile, at the outer boundary and at mid-depth of the spherical shell, at a snapshot in time near the end of the run-time for each of the four models. To compare with planetary flows the velocities are scaled in units of Rossby number $Ro = V_\phi/(\Omega r_o)$, which is the azimuthal component of the flow velocity in the rotating reference frame divided by the outer boundary equatorial rotation velocity. The peak cloud-level zonal flow velocities on Jupiter ($Ro \simeq 0.01$) and Saturn ($Ro \simeq 0.04$) occur near the equator. Noting that Model 1 has radius ratio $r_i/r_o = 0.9$ and Models 2, 3, and 4 have $r_i/r_o = 0.95$, and Jupiter and Saturn have estimated maximum depths of fast zonal flow at roughly $r/R_J \simeq 0.96$ and $r/R_S \simeq 0.86$, respectively (Liu et al., 2008; Heimpel and Gómeza Pérez, 2011; Kaspi et al., 2018; Galanti et al., 2019), we see that the flow velocities are in a range consistent with that of the gas giants. For all four runs, the similarity in strength of non-equatorial zonal flows at the outer boundary and at mid-shell depth shows that the jets are deeply seated. The equatorial zonal flows in Models 1 and 3 do show substantial variation of zonal flow velocity with depth. For Model 3 retrograde equatorial zonal flow at the outer boundary contrasts with prograde flow at mid-shell depth. As mentioned above, the parameters for Model 1 are the same as for

a previously published model (Heimpel et al., 2015), except that here, Model 1 was computed in a full sphere. Model 1 differs from the other models mainly in the radius ratio and the heating function, which concentrates buoyancy production (via the conductive entropy gradient ds_c/dr – see Fig. 3) at shallow levels below a thin stably stratified layer near the outer boundary. In contrast, Models 2, 3 and 4 have negative entropy gradients that do not peak at shallow levels. These models have relatively deep stably stratified layers, as indicated by the neutral stability radius, NSR (Table 1). In the deeper convective region, forcing increases with further depth toward the bottom boundary (Fig. 3). Thus Models 2 and 3, with deep stability in a relatively thin shell ($r_i/r_o = 0.95$) and a free-slip bottom boundary, yield zonal flows with a less dominant equatorial jet and relatively strong high latitude jets. Model 3 is the only simulation that has retrograde equatorial zonal flow. For the three cases with free-slip bottom boundary conditions, the prominence of a narrow equatorial zone of weaker prograde flow, which has previously been referred to as a "dimple" (Gastine et al., 2013; Garcia et al., 2019), increases with the depth of the NSR. We interpret the narrow band of equatorial retrograde flow in Model 3 as a strong dimple. Model 4 differs from the others in that it has a no-slip bottom boundary condition. This bottom condition efficiently quenches zonal flows at high latitudes. This is consistent with previous numerical deep convection studies that compare free-slip and mixed boundary conditions (Jones and Kuzanyan, 2009; Aurnou and Heimpel, 2004).
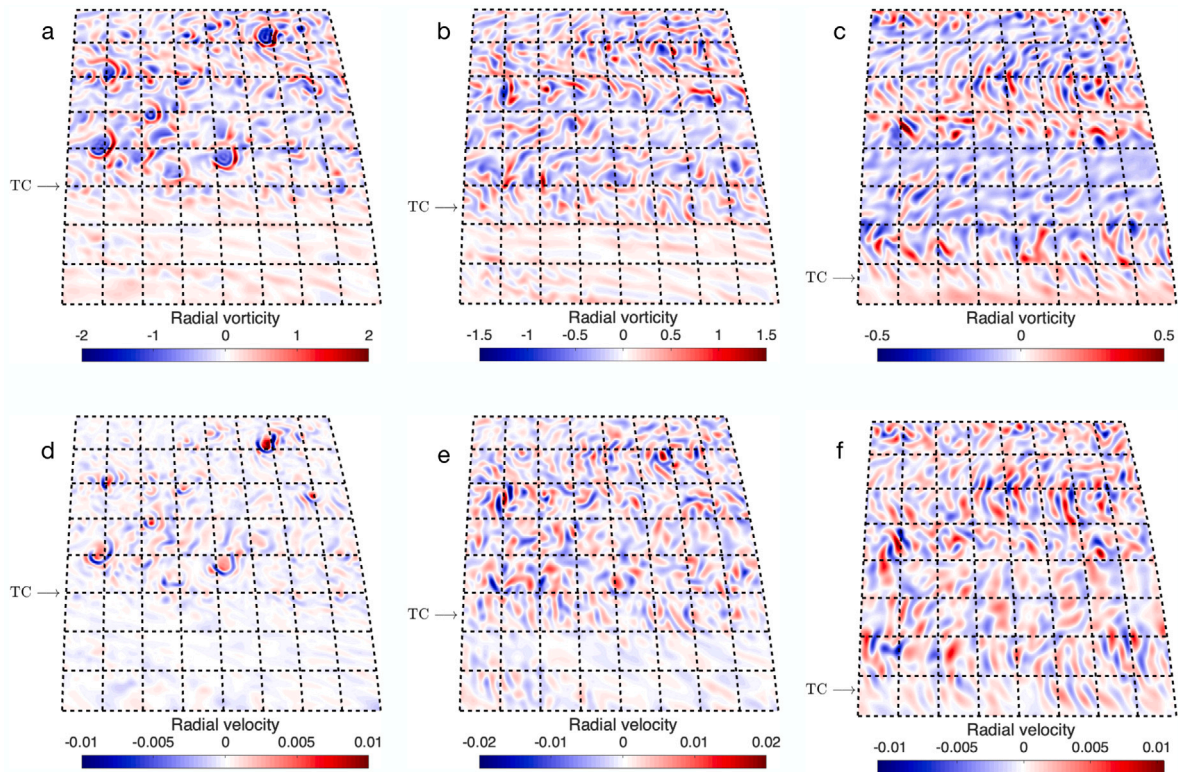
Fig. 10. Zoomed-in perspective view of radial vorticity (**a, b, c**) and radial velocity (**d, e, f**) at three different depths for Model 1 (compare to Fig. 5). The depths correspond to $r = 0.9991r_o$ (**a, d**), $r = 0.9856r_o$ (**b, e**) and $r = 0.9503r_o$ (**c, f**), with $r_i = 0.9r_o$. Dashed lines are longitude contours ranging from 145° to 169° and latitudes ranging from 16.8° to 40.8°. The 3° interval is similar in scale to Fig. 9. To locate this zoomed-in region, note that zero longitude is at 3 o'clock in Fig. 5. For each image, the latitude of the depth-dependent tangent cylinder $\lambda_{TC} = \cos^{-1}(r_i/r)$ is marked. At the outer boundary $\lambda_{TC} = \cos^{-1}(r_i/r_o) = 25.8°$. Because these images show the northern hemisphere cyclonic (anticyclonic) vorticity corresponds to red (blue) colours. (For interpretation of the references to colour in this figure legend, the reader is referred to the web version of this article.)

4.2. Three-dimensional thermal and flow structures

4.2.1. Global structures

Each of the Figs. 5–8 show images of the global thermal and flow structure of the four models. The models represent a range of depths, velocity boundary conditions, heating types, and Rayleigh & Ekman numbers (Table 1). Note that the velocity colour bar scale is in Rossby number based on shell depth $Ro_d = v/(\Omega d)$ for Figs. 5–8.

The width of the equatorial jet depends primarily on the shell depth (Model 1 has $r_i/r_o = 0.9$ while Models 2, 3 and 4 have $r_i/r_o = 0.95$). That width is a direct result of the 2-dimensionalization of quasi-geostrophic flow in a rapidly rotating fluid spherical shell (Heimpel et al., 2005). Prograde flow tends to fill the volume outside the tangent cylinder (TC), which is the imaginary axial cylinder tangent to the inner spherical surface. This can be seen clearly in the ϕ - slice images of axisymmetric zonal velocity in Figs. 5d–8d. Comparing Figs. 5–8 to Fig. 4 shows that the latitude that bounds the equatorial jet at the outer boundary is roughly given by the latitude of intersection of the TC with the outer boundary, $\lambda_{TC} = \cos^{-1}(r_i/r_o)$, i.e. $\lambda_{TC} \simeq 26°$ for $r_i/r_o = 0.9$ and $\lambda_{TC} \simeq 18°$ for $r_i/r_o = 0.95$. As mentioned above, we interpret the retrograde equatorial flow of Model 3 as a strong dimple on the prograde equatorial flow, which is bounded by the TC. Weaker equatorial dimples are also evident for Models 1 and 2, while Model 4 shows a different prograde equatorial flow structure.

Zonal flow is strongly cylindrical in all four models, as seen in Figs. 5d–8d. Furthermore, the radial vorticity does not depend strongly on depth in Models 2 and 3, which both have relatively deep stable stratification and free-slip bottom boundary conditions. This is seen by comparing the radial vorticity near the outer boundary and at mid-shell (Figs. 5c & f and 6c & f). Model 1 has stronger vorticity near the outer boundary than at mid-depth. This is due to the internal heating,

which in contrast to the other three models, features a forcing function (the conductive entropy gradient $-ds_c/dr$) that peaks near the outer boundary (see Fig. 3). Models 1, 2, and 3, which have free-slip top and bottom boundaries, have coherent zonal jets at all latitudes. This is evident in Figs. 4–7. As mentioned above, only the equatorial jet is coherent for Model 4. Fig. 8e shows that strong azimuthal flow velocity occurs in patches for Model 4, but this azimuthal flow is not axisymmetric, and does not form coherent zonal flows.

While all four models show small wavelength azimuthal patterns (typically of order 1°), which we interpret as sheared convection columns (see Jones et al. (2009)), Models 2 and 3 also have wave-like patterns of relatively large wavelength visible on the higher latitude polar jets. For Model 3 this wave-like pattern is most visible in Fig. 7e on the prograde jet near 55° latitude. Although none of these models formed a polar hexagon comparable to that of Saturn (see Yadav and Bloxham (2020)), Model 2 comes close to forming a polygonal pattern in the prograde jet near 60° latitude (Fig. 6e).

4.2.2. Polar and mid-latitude regions

For all four models we find that polar regions are characterized by cyclonic vortices, whereas mid-latitudes, particularly in the region near the TC, show preference for anticyclonic vortices. As discussed above, this may be discerned by comparing Figs. 5–8.

Zoomed-in comparisons of flow structure in the polar and mid-latitude regions are shown for Models 1 and 4 in Figs. 9–12. South polar region images of radial vorticity and radial velocity for Model 1 (Fig. 9) show the tendency for anticyclonic vortices to form at shallow depth, even near the poles. In Fig. 9 we see that the radial vorticity and velocity are strongly correlated at relatively shallow depths, and less so at greater depth. Thus, shallow anticyclones correspond to shallow upwelling, which is favoured for Model 1, given the strong shallow
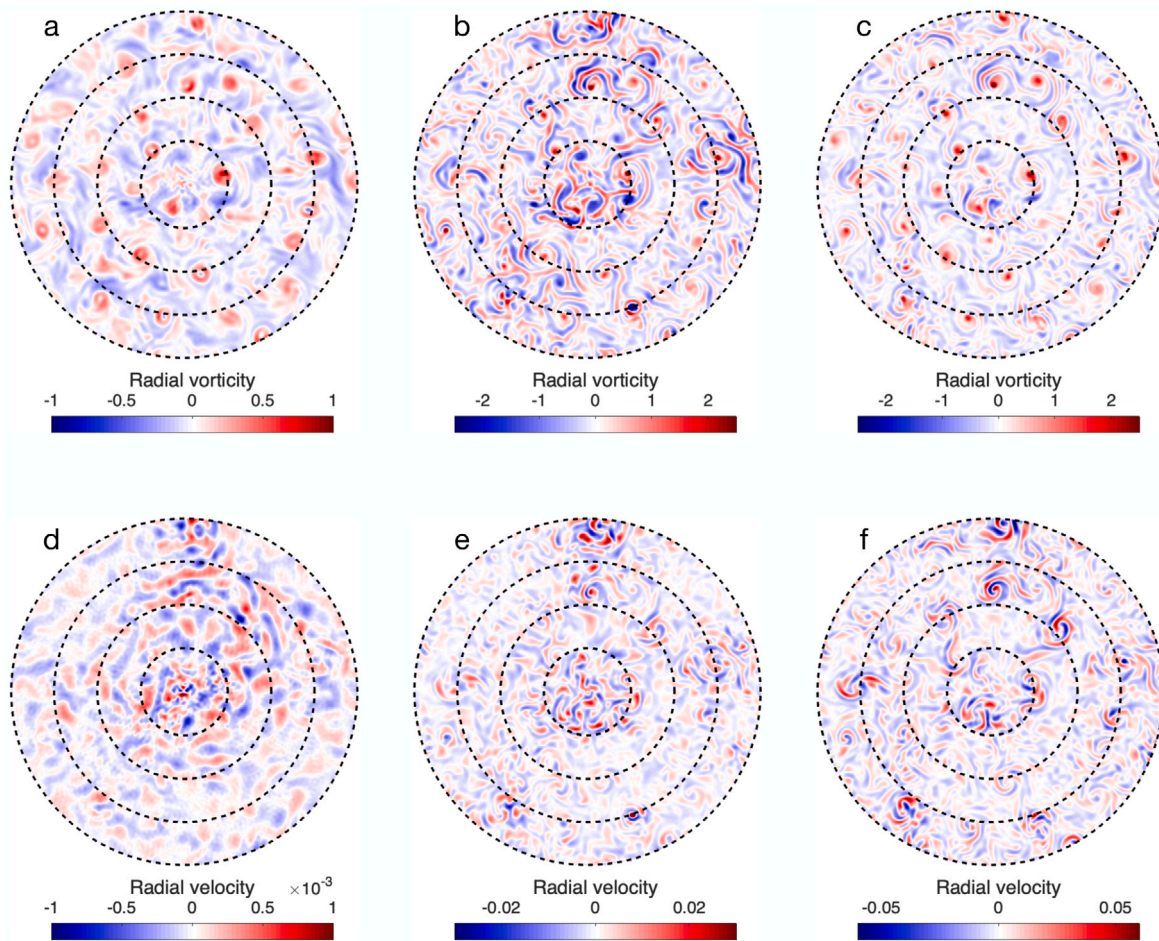
Fig. 11. Zoomed-in north polar view of radial vorticity (**a, b, c**) and radial velocity (**d, e, f**) at three different depths for Model 4 (compare to Fig. 8). The depths correspond to $r = 0.9995r_o$ (**a, d**), $r = 0.9927r_o$ (**b, e**) and $r = 0.975r_o$ (**c, f**), with $r_i = 0.95r_o$. Dashed contours show latitudes of 78°, 81°, 84°, 87°.

cooling that peaks at $r = 0.987$ in this model (see Fig. 3). In addition to the shallow anticyclones that occur at all latitudes for Model 1, we see in Fig. 9 a single polar cyclone that is deeply seated. We note that the south polar cyclone shown in Fig. 9 has a peak vorticity of about 0.2, which is 10% of the planetary vorticity, at all the depths output in the model. However, near the outer boundary, the typical radial vorticity of anticyclones and cyclonic filaments is more than an order of magnitude greater than that of the polar cyclone. Thus the colour scale in Fig. 9a, which is 10× that of Fig. 9b, c, obscures visualization of the polar cyclone. A single polar cyclone also exists in the northern hemisphere for Model 1. The north polar cyclone is not shown in Fig. 9, but can be discerned in Fig. 5. Comparing Models 1, 2 and 3, we find that Model 1 has relatively weak polar cyclones, with those of Models 2 and 3 having roughly four times and twice greater vorticity, respectively (see Figs. 6b, c,f, and 7b, c and f).

North mid-latitude region images of radial vorticity and radial velocity for Model 1 (Fig. 10) show the dominance of shallow anticyclones near the TC and at higher latitudes. Note that the radial vorticity of anticyclones increases with latitude, as the radial vorticity becomes aligned (or more precisely anti-aligned, for anticyclones) to the background vorticity at the pole. Coherent cyclones are not seen outside the polar regions. However, at all latitudes the shallow anticyclones are shielded by cyclonic rings and filaments (Heimpel et al., 2015). These shielded anticyclones are seen to be coherent and strongly correlated with the radial velocity at shallow depth, within the stably stratified layer. Vortical coherence and correlation to radial velocity is greatly diminished but still discernible in the convective zone, just below the stably stratified layer, and continues to diminish at greater

depth, where convectively-driven zonal flow dominates over vortex production. Comparing the images of radial vorticity in Fig. 10 for the three different depths (**a, b, c**) we see that the zonal jets follow a cylindrical pattern, with the first retrograde jet (or anticyclonic shear band) North of the equator bounded by the TC to the South (compare with Fig. 5(d).

Fig. 11 shows images of radial vorticity and radial velocity in the North polar region for Model 4. This model differs from the other three in that the velocity boundary conditions are mixed, with a no-slip bottom boundary. Comparing to Model 1, the heating conditions for Model 4 lack the strong negative entropy gradient near the base of the relatively shallow stably stratified layer (see Fig. 3). The images show the dominance of circumpolar cyclones (CPC) near the poles (see also Fig. 8). The cyclones are shown to be mostly continuous from near the outer boundary to mid-shell. Notably, the vorticity very near the outer boundary ($r = 0.9995r_o$) is strongly correlated with the midshell ($r = 0.975r_o$) vorticity, while the vorticity is less clearly correlated between $r = 0.9927r_o$ and the other two radii shown. At this depth, we see mix of cyclonic and anticyclonic vortices, with cyclonic and anticyclonic filaments. The vortical flow structure at $r = 0.9927$ corresponds strongly to the radial velocity, which is much stronger than the radial velocity at $r = 0.9995r_o$. Thus we see that strong upward flow close to the outer boundary gives rise to anticyclones. These anticyclones seem to locally (in terms of depth) modify the dominant cyclones, which remain as the encircling cyclonic filaments. Interestingly, these anticyclones are confined to the depth of relatively strong radial flow near the outer boundary, leaving the dominant cyclones at even shallower levels and at mid-shell depth strongly correlated with each other. Interpreting
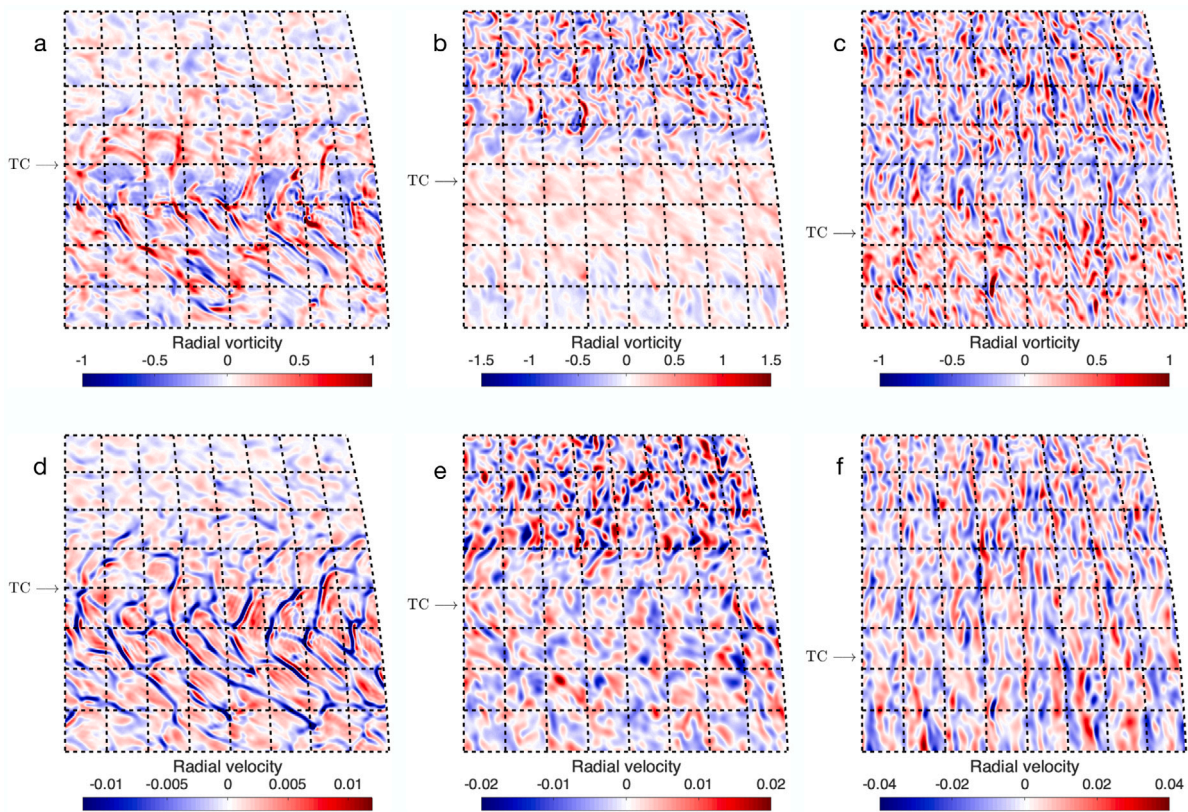
Fig. 12. Zoomed-in perspective view of radial vorticity (**a, b, c**) and radial velocity (**d, e, f**) at three different depths for Model 4 (compare to Fig. 8). The depths correspond to $r = 0.9995r_o$ (**a, d**), $r = 0.9927r_o$ (**b, e**) and $r = 0.975r_o$ (**c, f**), with $r_i = 0.95r_o$. Dashed lines are longitude contours ranging from 0° to 24° and latitudes ranging from 6.2° to 30.2°. The 3° interval is similar in scale to Figs. 9–12. For each image, the latitude of the depth-dependent tangent cylinder $\lambda_{TC} = \cos^{-1}(r_i/r)$ is marked. At the outer boundary $\lambda_{TC} = \cos^{-1}(r_i/r_o) = 18.2°$.

these results, we find that cyclones are the dominant vortices in the polar regions, but anticyclones form where strong upward flow diverges due to the proximity of the top boundary.

Fig. 12 shows images of radial vorticity and radial velocity in the mid-latitude region for Model 4. The depths are the same as for Fig. 11. As for the other models, we see little evidence of coherent cyclones in this latitude range near the TC. Anticyclones are evident, but they are not as circular nor coherent as those seen for Model 1 (Fig. 10). Comparing to Fig. 8d and e, we see that the retrograde jet is missing at the shallowest level ($r = 0.9995r_o$). Thus the relatively sharp northward transition from cyclonic to anticyclonic shear at the TC is not evident at the shallowest level (Fig. 12a and d). As for the polar region, coherent anticyclones are most evident at $r = 0.9927r_o$, where they correspond to relatively strong radial flow. Also at $r = 0.9927r_o$ anticyclones form just North of the TC, which corresponds to the first retrograde (anticyclonic shear) jet (see also Fig. 10). The cylindrical flow structure, at greater than the shallowest depths, is shown by the proximity of the first anticyclonic shear band, which is discernible just north of the TC in Fig. 12b and c.

4.3. Potential vorticity

Jet structures and the prevalence of vortices may be described in terms of conservation of potential vorticity (PV). Effective PV mixing leads to deviations from the uniform rotation planetary vorticity profile $2\Omega \sin \lambda$, where λ is the latitude. Planetary zonal flows featuring multiple jets form PV staircases, with reduced rotation rate (westward jets for eastward planetary rotation) corresponding to roughly constant PV steps, separated by steep rises at the eastward velocity peaks (Dunkerton and Scott, 2008; Marcus and Shetty, 2011; Heimpel et al., 2015). The reduced prograde velocity dimple of Jupiter's equatorial jet and the

retrograde velocity jets of Uranus and Neptune have been explained in terms of angular momentum mixing, a similar process by which strong convection mixes vorticity, yielding locally or globally retrograde zonal flows (Aurnou et al., 2007; Gastine et al., 2013). This angular momentum mixing explanation does not clearly apply to the equatorial dimples in our models, since our models include stable stratification, rather than strong convection, at shallow levels. Indeed, each of the dimples seen in Models 1, 2 and 3 has a latitudinal width that corresponds to a TC of depth roughly equal to that of the NSR (see Table 1 and Fig. 4). Thus we can interpret equatorial dimples in our models as arising from stability, or lack of convection. Future work will be needed to more clearly demonstrate the origin of jet dimples where stable stratification overlies convection.

We use two forms of PV to help analyse our results. The total radial vorticity (Fig. 13), defined as $WT_r(\lambda) = 2\Omega \sin \lambda + W_r(\lambda)$, where $W_r(\lambda)$ is the azimuthally averaged radial vorticity in the rotating frame, has been used as a simple proxy for PV (Dunkerton and Scott, 2008; Heimpel et al., 2015). The cylindrical potential vorticity (Fig. 14) is defined as $PV_z(s) = (2\Omega + W_z(s))/h(s)$, where 2Ω is the background vorticity of solid body rotation, $W_z(s)$ is the azimuthally averaged axial vorticity in the rotating frame, and $h(s)$ is the fluid column length in the axial direction as a function of distance from the rotation axis s (cylindrical radius). This $PV_z(s)$ is a form of topographic PV applied in the axial (rather than radial) direction to spherical geometry (Pedlosky, 1987; Yano et al., 2005; Heimpel and Aurnou, 2007). Both WT_r and PV_z may be considered approximations since neither includes the vorticity contribution from fluid compression (Gastine et al., 2014a).

Comparing Figs. 13 and 14, $WT_r(\lambda)$ and $PV_z(s)$ look quite different. However, this is largely due to the difference between the horizontal axes. Whereas WT_r is plotted as a function of the latitude λ, PV_z is plotted as a function of the cylindrical radius $s = r \cos \lambda$. The
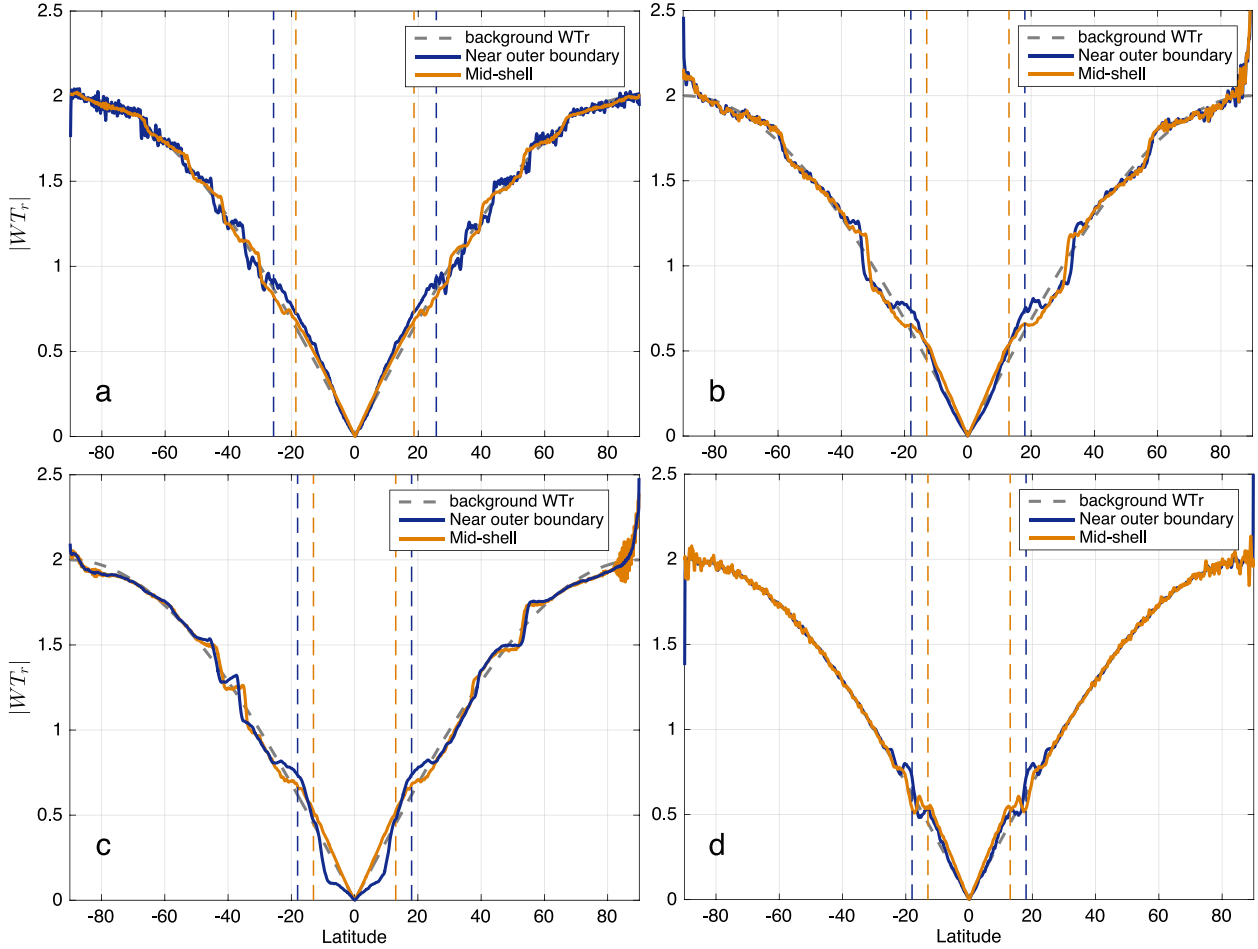
Fig. 13. Absolute value of the total radial vorticity $|WT_r|$ in units of background rotation rate Ω for Models 1, 2, 3 and 4 (a, b, c, d, respectively). Grey dashed lines give the background total radial vorticity $2\sin\lambda$. Blue solid lines give $|WT_r|$ at $r/r_o = 0.999$. Orange solid lines give $|WT_r|$ at mid-shell radius ($r/r_o = 0.95$ for Model 1, $r/r_o = 0.975$ for Models 2, 3 and 4). Thin blue and orange dashed lines give the latitudes of the tangent cylinder at these radii $\lambda_{TC} = \cos^{-1}(r_i/r)$ for each model. (For interpretation of the references to colour in this figure legend, the reader is referred to the web version of this article.)

relationship between the two functions is seen by noting that $1/h(\lambda) = \sin\lambda$ in the limit of $r_i/r_o \simeq 1$ (thin layer). Thus WT_r and PV_z are identical in the limit of zero shell thickness. For the relatively thin shells of our models ($r_i/r_o = 0.9 - 0.95$) the two functions are approximately equal inside the TC. However, whereas WT_r is continuous for the full range of λ and s, PV_z is discontinuous, due to the discontinuity in h across the tangent cylinder (Heimpel and Aurnou, 2007).

The advantage of PV_z is that, for quasi-geostrophic flows with cylindrical geometry, it takes into account flow over the full depth range in a spherical shell. A utility of WT_r is that it provides a direct connection to cyclones and anticyclones, which are the radial vorticity structures observed at the cloud level of Jupiter and Saturn. Thus, as noted above, WT_r may be considered a measure of potential vorticity for flow in very thin layer, such as the stably stratified layer near the outer boundary. In that sense, and because it is continuous across the TC, WT_r is easier to interpret than PV_z, particularly across and outside the TC. Fig. 13 shows $|WT_r|$ near the outer boundary, at $r/r_o = 0.999$ and at mid-shell depth for our four models.

As may be seen in Fig. 4, Models 1 and 2 have dimples on their prograde equatorial jets at the outer boundary, but lack equatorial dimples at midshell depth. The dimples correspond to slight reduction in the WT_r slope at the outer boundary (blue lines in Fig. 13). Little or no reduction of mid-shell depth WT_r slope (orange lines) is consistent with the lack of dimples at depth. Model 3 features a retrograde equatorial jet at the outer boundary, and a prograde jet at mid-shell depth. This corresponds to sharply reduced outer boundary WT_r slope

centred on the equator, with no such reduction at mid-shell depth. Model 4 displays no dimple on its equatorial jet, and no significant reduction of WT_r slope is found.

Reduced slope steps of WT_r and PV_z at higher (mid-) latitudes correspond to retrograde jets (Figs. 13 and 14). The relatively constant potential vorticity steps form a background in which anticyclones are most prevalent (Heimpel et al., 2015). Model 1 shows most clearly the tendency for anticyclonic vortices to form in the retrograde jets at mid and high latitudes. There are five retrograde jets in each hemisphere for Model 1, each with a corresponding step of reduced WT_r and PV_z. Model 3 also shows strong WT_r and PV_z steps, particularly the two steps near the latitude range $45° < \lambda < 60°$, which corresponds to the cylindrical radius range $0.5 < s < 0.7$ in the northern hemisphere. Models 2 and 3 show the strongest tendency to form polar cyclones, which occur in all four models (see Figs. 5–9, 11) . Whereas Models 2 and 3 have strong, single polar cyclones in each hemisphere, for both models, the alignment with the rotation axes in the North is stronger than in the South. Thus we see a strong rise in WT_r and PV_z toward the pole, both at the outer boundary and at mid-shell depth in the Northern hemisphere for both models. This strong rise in potential vorticity at the poles looks like the rises between relatively constant steps of WT_r and PV_z. However, we see, especially in Models 2 and 3, that this rise in potential vorticity can be anomalously strong at the pole. This description of polar WT_r and PV_z is consistent with the qualitative interpretation of polar cyclones being prograde jets, centred on the rotation axis. However, circumpolar cyclones (CPC) occur in all of the
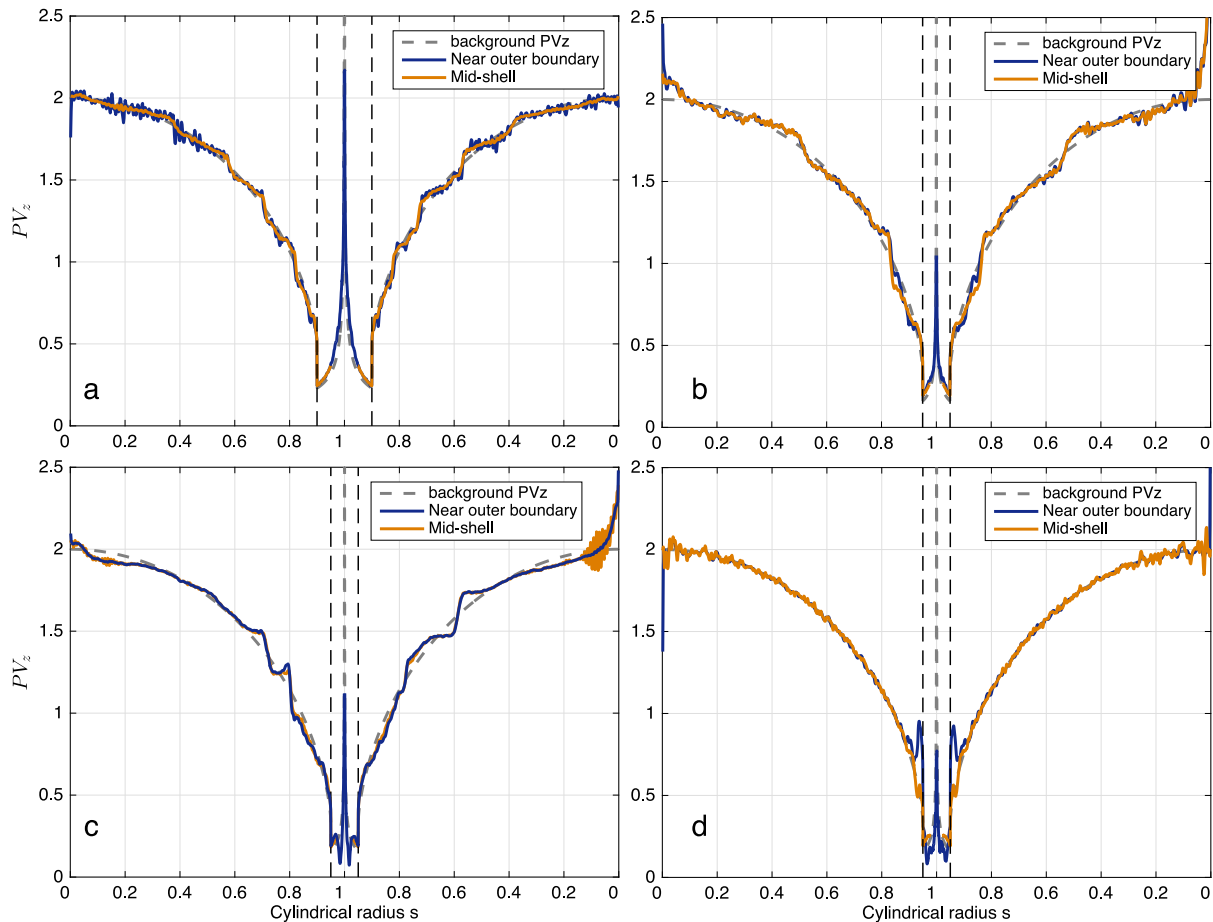
Fig. 14. Cylindrical potential vorticity PV_z in units of background rotation rate Ω. Grey dashed lines give the background cylindrical potential vorticity $2/h(s)$. Blue solid lines give PV_z at $r/r_o = 0.999$. Orange solid lines give PV_z at mid-shell radius ($r/r_o = 0.95$ for Model 1, $r/r_o = 0.975$ for Models 2, 3 and 4). The thin black dashed line gives the value of s at the tangent cylinder radius $s_{TC} = r_i$ for each model. (For interpretation of the references to colour in this figure legend, the reader is referred to the web version of this article.)

models, and none of the single polar cyclones are perfectly centred on the axis of rotation. Although the relatively short timescale of our models (see Table 1) precludes significant latitudinal drift of individual vortices in our models, the prevalence of off-axis and multiple polar cyclones in all of our models is consistent with the idea of beta-drift (Li et al., 2020; O'Neill et al., 2015; Scott, 2011).

4.4. Power spectra

Fig. 15 shows power spectra of the kinetic energy near the outer boundary and at mid-shell depth for each of the four models. All models show strong peaks for even-numbered harmonics, starting with degree $l = 2$ (quadrupole). To interpret these spectra we consider three idealized jet profiles (shown in Fig. 16) and compute the spherical harmonic spectra (Fig. 17) that correspond to the simple profiles.

The *Mid-Lat Jets* profile lacks a prograde equatorial jet, and has several higher latitude jets, alternating in the retrograde and prograde directions, with a wavelength $\lambda = \pi/9$, or 20° in latitude. The *Equatorial Jets* profile has a prograde jet and two retrograde jets near the equator, and lacks higher latitude jets. The *Full Profile* has jets at all latitudes, corresponds to the *Equatorial Jets* profile near the equator, and corresponds to *Mid-Lat Jets* at higher latitudes.

The three idealized zonal flow profiles of Fig. 16 may be compared to the four zonal flow profiles shown in Fig. 4. Qualitatively, the profiles of Model 1 and Model 2 resemble the idealized *Full Jet* profile, the Model 3 profile resembles *Mid-Lat Jets*, and Model 4 resembles *Equatorial Jets*.

Fig. 17 shows a comparison of the model spectra with spectra for the idealized jet models with linear axes ranging from degree 1 to 40. Although Model 1 has high latitude jets of significant amplitude, the kinetic energy at the outer boundary is dominated by the equatorial jet. This explains why the Model 1 spectrum is not well fit by the *Full Profile* spectrum, but rather looks more like the *Equatorial Jets* spectrum. The Model 2 and *Full Profile* spectra are quite similar. Both represent profiles in which high latitude and equatorial jets have roughly equal kinetic energy. The Model 3 and *Mid-Lat Jets* profiles are also quite similar, due to the similar profiles with strong high latitude jets and relatively weaker equatorial zonal flow. The simplest comparison is perhaps between Model 4 and *Equatorial Jets*. Comparing Figs. 4 to 16, we see that both profiles lack high latitude jets. However, whereas the *Equatorial Jets* profile has a pair of retrograde jets near the prograde equatorial jet, Model 4 zonal flow at the outer boundary lacks retrograde jets. Thus, the idealized profile spectrum has more even degree peaks (up to degree 20) than the Model 4 spectrum.

5. Discussion and conclusions

Our models represent a range of atmospheric stability conditions, from relatively shallow to deeper stable stratification, and two different bottom velocity boundary conditions (free-slip and no-slip). For all cases we find that surface jets project into the interior cylindrically, which has been shown in previous Boussinesq models (Heimpel et al., 2005) and for anelastic models with strong density stratification (e.g., Gastine et al. (2014a) and Heimpel et al. (2015)). As for those
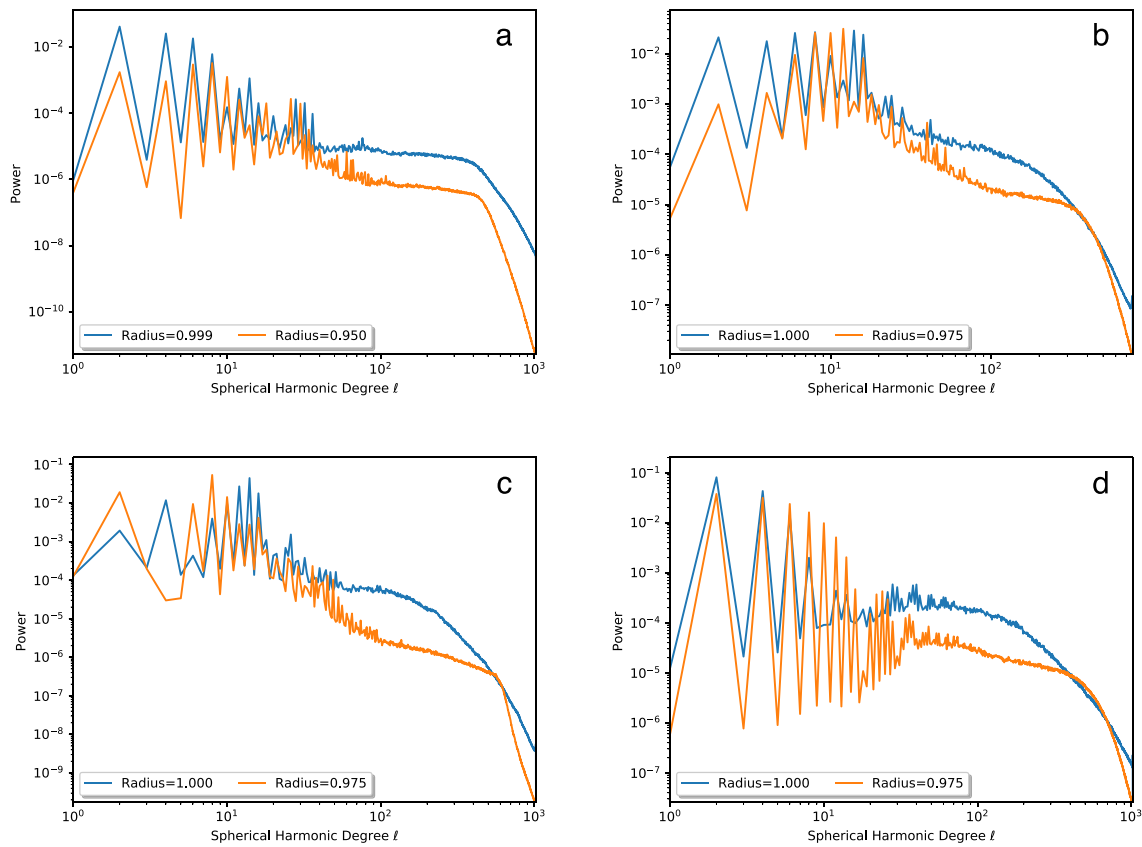
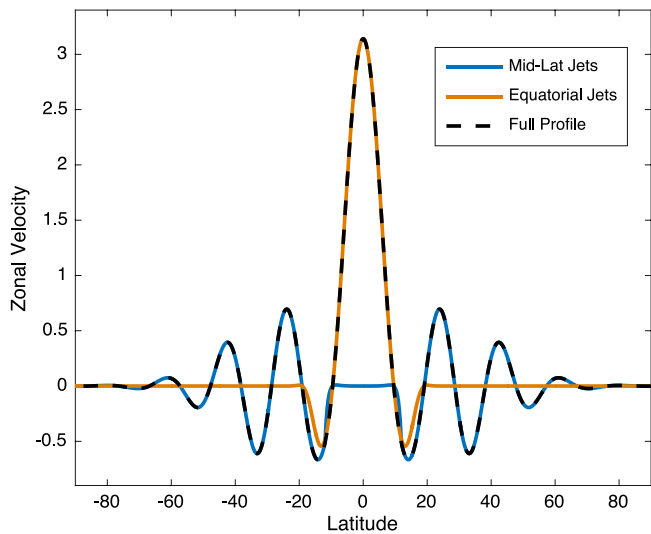**Fig. 15.** Spectra for the four models. a, Model 1. b, Model 2. c, Model 3. d, Model 4.

Fig. 16. Three idealized Zonal Flow Profiles. The black dashed (Full) profile represents zonal flow with equatorial and higher latitude jets. The blue profile (Mid-Lat Jets) has the equatorial jet removed. The orange profile (Equatorial Jets) has higher latitude jets removed, leaving the prograde and two retrograde jets near the equator. (For interpretation of the references to colour in this figure legend, the reader is referred to the web version of this article.)

previous results, our current models show deep jets with mostly strong symmetry about the equator. However, as Model 3 shows, differences in the zonal flow velocities of mid-latitude jets do occur as well, which is consistent with significantly elevated odd harmonic power in the kinetic energy spectrum (see Figs. 4 and 9). This model also has

the deepest near-surface stable layer (Fig. 3), and shallow retrograde flow at the equator, perhaps comparable with the features of Jupiter's atmosphere: strong stability conditions and jet asymmetry. As argued in Section 4.3, the band of retrograde zonal velocity centred on the equatorial jet may be interpreted as being comparable to the dimple of slower prograde flow on Jupiter.

A central finding of this work concerns the variation of occurrence of cyclonic and anticyclonic vortices with latitude and depth in our models. Images of radial vorticity ω_r are shown near the outer boundary and at mid-depth for all four models (Figs. 5–8, c & f). These images show the prevalence of anticyclonic vorticity at shallow depths and low latitudes, and the prevalence of cyclonic vorticity near the poles. Comparing Fig. 4 (zonal flow profiles) to Fig. 5c–f (ω_r near the outer boundary), cyclonic vortices are seen to occur at latitudes greater than the equatorial jet. Anticyclonic vorticity is favoured within the first anticyclonic region of shear outside the equatorial jet. A strong decrease in radial anticyclonic vorticity is particularly prevalent at low latitudes for Models 1–3. All four models also show the tendency for anticyclones to be shielded by filaments of cyclonic vorticity, especially at mid-latitudes. These shielded vortices were previously described in numerical models (Heimpel et al., 2015) and observational models of Jupiter's atmosphere (de Pater et al., 2010).

The simulations confirm that anticyclonic vortices form preferentially at low latitudes, especially within the first anticyclonic shear away from the equatorial jet (Heimpel et al., 2015). Previous models have shown that cyclonic vortices drift preferentially toward the poles (beta-drift) (Li et al., 2020; O'Neill et al., 2015; Scott, 2011). We find that deep convection leads to a variable pattern of vorticity in depth as well as latitude, with shallow anticyclonic vortices favoured at mid-latitudes and deeply seated cyclones near the poles. Consistent with (Heimpel et al., 2015) we find that the mid-latitude anticyclones are much stronger at shallow depths than at mid-shell levels. This is explained as a boundary effect; the anticyclones are formed by
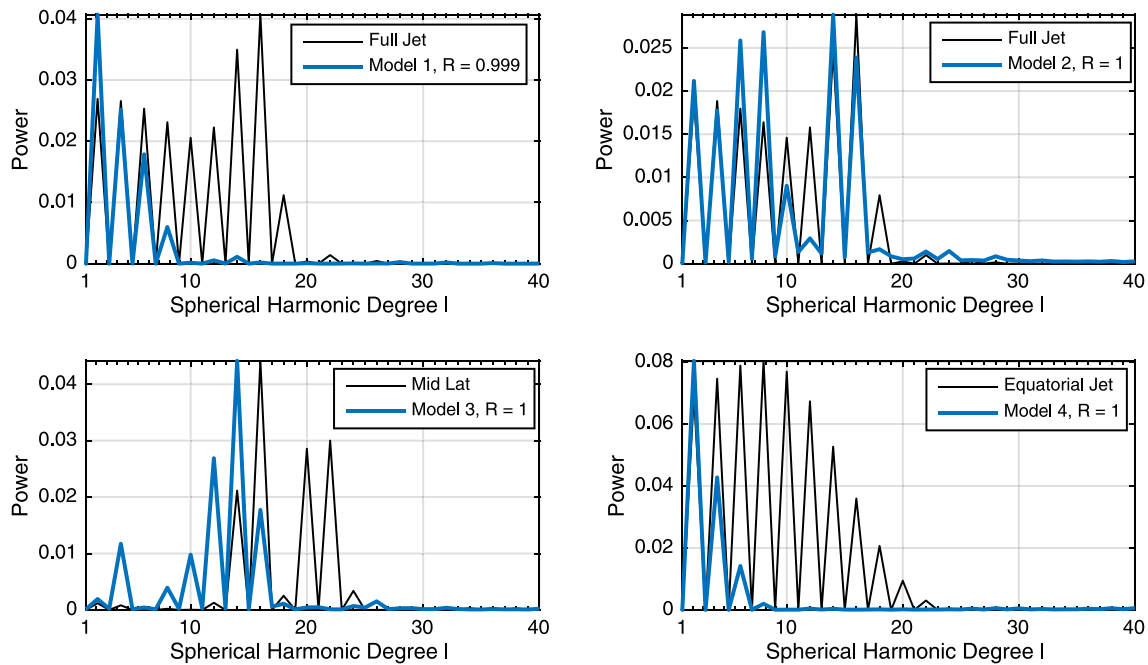
Fig. 17. Comparison of idealized jet spectra with spectra of kinetic energy near the outer boundary for the four models.

upwellings that originate in the convective zone and diverge near and at the top boundary. In contrast, we find that the polar and high latitude cyclones are deeply seated, with little or no reduction of vorticity with depth (or increasing vorticity with depth for Model 4). The full depth extent of a polar vortex may be explained by considering it as a prograde (cyclonic) jet centred on the polar axis. This is clearly seen by examining the zonal velocity in Fig. 4. Models 2 and 3 each have a polar jet with prograde velocity declining to zero at the pole. These polar vortices are shown as steep rises in WT_r and PV_z (Figs. 13 and 14). This relationship between polar jet and deep seated cyclonic vortex may also be seen in Figs. 5–8, by examining the velocity and vorticity fields, especially for Models 2 and 3 (compare Figs. 6e to c, f and 7e to c, f).

Cyclones dominate in the polar regions of all four models. In contrast to the shallow anticyclones, these polar cyclones are deeply seated, suggesting that the shallow stable layer does not play a role in their formation. A single, more or less pole-centred cyclone occurs in each hemisphere of the three models with free slip boundary conditions (Models 1, 2, 3), whereas clusters of circumpolar cyclones (CPC) occur in both polar regions for Model 4 has mixed velocity boundary conditions (free-slip top and no-slip bottom), which result in relatively weak and non-axisymmetric zonal flows at high latitudes. The inhibition of zonal flow by no-slip bottom boundaries was shown previously (Aurnou and Heimpel, 2004). Spherical dynamo models of the gas giants have shown a similar effect: the deep dynamo disallows fast zonal flows to develop in the deep interior, and at high latitudes (Heimpel and Gómeza Pérez, 2011; Gastine et al., 2014b). However, laboratory experiments on rotating flows with height that varies with cylindrical radius have shown that strong jets may form in the presence of a zero bottom boundary velocity (no-slip) condition (Lemasquerier et al., 2021; Cabanes et al., 2017). The weak higher latitude zonal flows of Model 4 may favour the occurrence of CPC. Another possibility is that the strength of forcing determines the polar vorticity regime. Model 4 also has the strongest forcing of the four models. With the no-slip bottom boundary condition, strong forcing was required to produce an equatorial jet of comparable velocity ($Ro \sim 0.01$ – see Fig. 4) to the other models, which employed free-slip top and bottom boundary conditions.

While our models exhibit wave-like features on the zonal flows at high latitudes, particularly in Models 2 and 3 (see Figs. 6 and 7),

polygonal patterns are transient and not as clear as Saturn's north polar hexagonal jet. The Saturn hexagon has been modelled in previous deep convection models as arising due to persistent, large scale vortices that deflect zonal flow (Yadav and Bloxham, 2020).

Model 4, which has the strongest convective forcing, has several cyclones at each pole, comparable to Jupiter. This is consistent with previous findings using models driven by moist convection (O'Neill et al., 2015). These cyclones are not centred on the polar axis and cannot be interpreted as polar jets. The greater depth extent of polar cyclones, and high latitude anticyclones, may be due to the alignment of thermal plumes with the rotation axis in the polar regions (Aurnou et al., 2008). (For an example of a deeply seated anticyclone in the polar region see Fig. 6c and f.)

Rapid progress in understanding the deep dynamics of Jupiter and Saturn has come from the Juno and Cassini missions. However, much uncertainty exists about the radial profiles of Hydrogen dissociation, stability stratification, and the role of Helium. Future modelling that explores the truncation of cylindrical zonal flows in the transition from the molecular envelope to the deeper dynamo will help us gain further understanding of the structure and dynamics of the deep interiors and atmospheres of the giant planets.

CRediT authorship contribution statement

Moritz H. Heimpel: Simulations, Writing – original draft, Created the figures. **Rakesh K. Yadav:** Writing – review & editing. **Nicholas A. Featherstone:** Developed the computational dynamo code Rayleigh, Helped create figures, Made data hosting possible, Writing – review & editing. **Jonathan M. Aurnou:** Writing – review & editing.

Declaration of competing interest

The authors declare that they have no known competing financial interests or personal relationships that could have appeared to influence the work reported in this paper.

Acknowledgements

References

Adriani, A., Mura, A., Orton, G., Hansen, C., Altieri, F., Moriconi, M., Rogers, J., Eichstädt, G., Momary, T., Ingersoll, A.P., et al., 2018. Clusters of cyclones encircling Jupiter's poles. Nature 555 (7695), 216–219.

Aurnou, J.M., Heimpel, M., 2004. Zonal jets in rotating convection with mixed mechanical boundary conditions. Icarus 169, 492–498.

Aurnou, J., Heimpel, M., Allen, L., King, E., Wicht, J., 2008. Convective heat transfer and the pattern of thermal emission on the gas giants. Geophys. J. Int. 173 (3), 793–801.

Aurnou, J., Heimpel, M., Wicht, J., 2007. The effects of vigorous mixing in a convective model of zonal flow on the ice giants. Icarus 190 (1), 110–126.

Brueshaber, S.R., Sayanagi, K.M., Dowling, T.E., 2019. Dynamical regimes of giant planet polar vortices. Icarus 323, 46–61.

Cabanes, S., Aurnou, J., Favier, B., Lea Bars, M., 2017. A laboratory model for deep-seated jets on the gas giants. Nat. Phys..

Cai, T., Chan, K.L., Mayr, H.G., 2021. Deep, closely packed, long-lived cyclones on Jupiter's poles. Planet. Sci. J. 2 (2), 81.

Cao, H., Stevenson, D.J., 2017. Zonal flow magnetic field interaction in the semi-conducting region of giant planets. Icarus 296, 59–72.

Christensen, U.R., Wicht, J., Dietrich, W., 2020. Mechanisms for limiting the depth of zonal winds in the gas giant planets. Astrophys. J. 890 (1), 61.

de Pater, I., Wong, M.H., Marcus, P., Luszcz-Cook, S., Ádámkovics, A., Asay-Davis, X., Go, C., 2010. Persistent rings in and around Jupiter's anticyclones–observations and theory. Icarus 210 (2), 742–762.

Dougherty, M.K., Cao, H., Khurana, K.K., Hunt, G.J., Provan, G., Kellock, S., Burton, M.E., Burk, T.A., Bunce, E.J., Cowley, S.W., et al., 2018. Saturn's magnetic field revealed by the Cassini Grand Finale. Science 362 (6410), 1–11.

Duarte, L., Wicht, J., Gastine, T., 2018. Physical conditions for Jupiter-like dynamo models. Icarus 299, 206–221.

Duer, K., Gavriel, N., Galanti, E., Kaspi, Y., Fletcher, L.N., Guillot, T., Bolton, S.J., Levin, S.M., Atreya, S.K., Grassi, D., et al., 2021. Evidence for multiple ferrel-like cells on Jupiter. Geophys. Res. Lett. 48 (23), e2021GL095651.

Dunkerton, T.J., Scott, R.K., 2008. A barotropic model of the angular momentum-conserving potential vorticity staircase in spherical geometry. J. Atmos. Sci. 65 (4), 1105–1136.

Featherstone, N.A., Heimpel, M.H., Hindman, B.W., Matilsky, L., 2021. Rayleigh simulation library. http://dx.doi.org/10.17605/OSF.IO/J275Z.

Featherstone, N.A., Hindman, B.W., 2016. The spectral amplitude of stellar convection and its scaling in the high-Rayleigh-number regime. Astrophys. J. 818 (1), 32.

French, M., Becker, A., Lorenzen, W., Nettelmann, N., Bethkenhagen, M., Wicht, J., Redmer, R., 2012. Ab initio simulations for material properties along the Jupiter adiabat. Astrophys. J. Suppl. Ser. 202 (1), 5–15, [Online]. Available: http://stacks.iop.org/0067-0049/202/i=1/a=5.

Galanti, E., Kaspi, Y., Miguel, Y., Guillot, T., Durante, D., Racioppa, P., Iess, L., 2019. Saturn's deep atmospheric flows revealed by the Cassini Grand Finale gravity measurements. Geophys. Res. Lett. 46 (2), 616–624.

Garcia, F., Chambers, F., Watts, A., 2019. Polar waves and chaotic flows in thin rotating spherical shells. Phys. Rev. Fluids 4 (7), 074802.

Garcia, F., Chambers, F.R., Watts, A.L., 2020. Deep model simulation of polar vortices in gas giant atmospheres. Mon. Not. R. Astron. Soc. 499 (4), 4698–4715.

Gastine, T., Heimpel, M., Wicht, J., 2014a. Zonal flow scaling in rapidly-rotating compressible convection. Phys. Earth Planet. Inter. 232, 36–50.

Gastine, T., Wicht, J., 2012. Effects of compressibility on driving zonal flow in gas giants. Icarus 219 (1), 428–442.

Gastine, T., Wicht, J., 2021. Stable stratification promotes multiple zonal jets in a turbulent jovian dynamo model. Icarus 114514.

Gastine, T., Wicht, J., Aurnou, J., 2013. Zonal flow regimes in rotating spherical shells: An application to giant planets. Icarus 225, 156–172. http://dx.doi.org/10.1016/j.icarus.2013.02.031.

Gastine, T., Wicht, J., Duarte, L., Heimpel, M., Becker, A., 2014b. Explaining Jupiter's magnetic field and equatorial jet dynamics. Geophys. Res. Lett. 41 (15), 5410–5419.

Grassi, D., Adriani, A., Moriconi, M., Mura, A., Tabataba-Vakili, F., Ingersoll, A., Orton, G., Hansen, C., Altieri, F., Filacchione, G., et al., 2018. First estimate of wind fields in the Jupiter polar regions from JIRAM-Juno images. J. Geophys. Res.: Planets 123 (6), 1511–1524.

Guillot, T., Miguel, Y., Militzer, B., Hubbard, W.B., Kaspi, Y., Galanti, E., Cao, H., Helled, R., Wahl, S., Iess, L., et al., 2018. A suppression of differential rotation in Jupiter's deep interior. Nature 555 (7695), 227–230.

Heimpel, M., Aurnou, J., 2007. Turbulent convection in rapidly rotating spherical shells: A model for equatorial and high latitude jets on Jupiter and Saturn. Icarus 187 (2), 540–557.

Heimpel, M., Aurnou, J., Wicht, J., 2005. Simulation of equatorial and high-latitude jets on Jupiter in a deep convection model. Nature 438, 193–196.

Heimpel, M., Gastine, T., Wicht, J., 2015. Simulation of deep-seated zonal jets and shallow vortices in gas giant atmospheres. Nat. Geosci..

Heimpel, M., Gómeza Pérez, N., 2011. On the relationship between zonal jets and dynamo action in giant planets. Geophys. Res. Lett. 38 (14), 14201–14206.

Hubbard, W.B., 1999. Gravitational signature of Jupiter's deep zonal flows. Icarus 137 (2), 357–359.

Ingersoll, A.P., Dowling, T.E., Gierasch, P.J., Orton, G.S., Read, P.L., Sánchez-Lavega, A., Showman, A.P., Simon-Miller, A.A., Vasavada, A.R., 2004. Dynamics of Jupiter's atmosphere. Jupiter: Planet Satell. Magnetos. 105, 105–128.

Jones, C., 2014. A dynamo model of Jupiter's magnetic field. Icarus 241, 148–159.

Jones, C.A., Kuzanyan, K.M., 2009. Compressible convection in the deep atmospheres of giant planets. Icarus 204, 227–238.

Jones, C., Kuzanyan, K., Mitchell, R., 2009. Linear theory of compressible convection in rapidly rotating spherical shells, using the anelastic approximation. J. Fluid Mech. 634, 291–319.

Kaspi, Y., Flierl, G.R., Showman, A.P., 2009. The deep wind structure of the giant planets: Results from an anelastic general circulation model. Icarus 202, 525–542.

Kaspi, Y., Galanti, E., Hubbard, W.B., Stevenson, D., Bolton, S., Iess, L., Guillot, T., Bloxham, J., Connerney, J., Cao, H., et al., 2018. Jupiter's atmospheric jet streams extend thousands of kilometres deep. Nature 555 (7695), 223–226.

Kuang, W., Bloxham, J., 1999. Numerical modeling of magnetohydrodynamic convection in a rapidly rotating spherical shell: Weak and strong field dynamo action. J. Comput. Phys. 153, 51–81.

Lantz, S.R., Fan, Y., 1999. Anelastic magnetohydrodynamic equations for modeling solar and stellar convection zones. Astrophys. J. Suppl. Ser. 121, 247–264.

Lemasquerier, D., Favier, B., Lea Bars, M., 2021. Zonal jets at the laboratory scale: hysteresis and rossby waves resonance. J. Fluid Mech. 910.

Li, C., Ingersoll, A., Klipfel, A., Brettle, H., 2020. Modeling the stability of polygonal patterns of vortices at the poles of Jupiter as revealed by the Juno spacecraft. Proc. Natl. Acad. Sci. http://dx.doi.org/10.1073/pnas.2008440117.

Liu, J., Goldreich, P.M., Stevenson, D.J., 2008. Constraints on deep-seated zonal winds inside Jupiter and Saturn. Icarus 196 (2), 653–664.

Magalhães, J.A., Seiff, A., Young, R.E., 2002. The stratification of Jupiter's troposphere at the Galileo probe entry site. Icarus 158 (2), 410–433.

Marcus, P.S., Shetty, S., 2011. Jupiter's zonal winds: are they bands of homogenized potential vorticity organized as a monotonic staircase?. Phil. Trans. R. Soc. A 369 (1937), 771–795.

Matsui, H., Heien, E., Aubert, J., Aurnou, J.M., Avery, M., Brown, B., Buffett, B.A., Busse, F., Christensen, U.R., Davies, C.J., et al., 2016. Performance benchmarks for a next generation numerical dynamo model. Geochem. Geophys. Geosyst. 17 (5), 1586–1607.

Militzer, B., Soubiran, F., Wahl, S.M., Hubbard, W., 2016. Understanding Jupiter's interior. J. Geophys. Res.: Planets 121 (9), 1552–1572.

Moore, K.M., Yadav, R.K., Kulowski, L., Cao, H., Bloxham, J., Connerney, J.E., Kotsiaros, S., Jørgensen, J.L., Merayo, J.M., Stevenson, D.J., et al., 2018. A complex dynamo inferred from the hemispheric dichotomy of Jupiter's magnetic field. Nature 561 (7721), 76.

Nellis, W.J., Weir, S.T., Mitchell, A.C., 1999. Minimum metallic conductivity of fluid hydrogen at 140 GPa (1.4 mbar).. Phys. Rev. B 59 (5), 3434–3449.

O'Neill, M.E., Emanuel, K.A., Flierl, G.R., 2015. Polar vortex formation in giant-planet atmospheres due to moist convection. Nat. Geosci. 8 (7), 523–526.

Pedlosky, J., 1987. Geophysical Fluid Dynamics. Springer.

Sayanagi, K.M., Dyudina, U.A., Ewald, S.P., Fischer, G., Ingersoll, A.P., Kurth, W.S., Muro, G.D., Porco, C.C., West, R.A., 2013. Dynamics of Saturn's great storm of 2010–2011 from Cassini ISS and RPWS. Icarus 223 (1), 460–478.

Scott, R., 2011. Polar accumulation of cyclonic vorticity. Geophys. Astrophys. Fluid Dyn. 105 (4–5), 409–420.

Siegelman, L., Klein, P., Ingersoll, A.P., Ewald, S.P., Young, W.R., Bracco, A., Mura, A., Adriani, A., Grassi, D., Plainaki, C., et al., 2022. Moist convection drives an upscale energy transfer at jovian high latitudes. Nat. Phys. 1–5.

Starchenko, S.V., Jones, C.A., 2002. Typical velocities and magnetic field strengths in planetary interiors. Icarus 157, 426–435.

Stevenson, D., Salpeter, E., 1977a. The dynamics and helium distribution in hydrogen-helium fluid planets. Astrophys. J. Suppl. Ser. 35, 239–261.

Stevenson, D., Salpeter, E., 1977b. The phase diagram and transport properties for hydrogen-helium fluid planets. Astrophys. J. Suppl. Ser. 35 (10), 221–237.

Vasavada, A., Hörst, S., Kennedy, M., Ingersoll, A., Porco, C., Dela Genio, A., West, R., 2006. Cassini imaging of Saturn: Southern hemisphere winds and vortices. J. Geophys. Res.: Planets 111 (E5), 1991–2012.

Vasavada, A.R., Showman, A.P., 2005. Jovian atmospheric dynamics: An update after Galileo and Cassini. Rep. Progr. Phys. 68 (8), 1935–1996.

Wahl, S.M., Hubbard, W.B., Militzer, B., Guillot, T., Miguel, Y., Movshovitz, N., Kaspi, Y., Helled, R., Reese, D., Galanti, E., et al., 2017. Comparing Jupiter interior structure models to Juno gravity measurements and the role of a dilute core. Geophys. Res. Lett. 44 (10), 4649–4659.

Wicht, J., Gastine, T., 2020. Numerical simulations help revealing the dynamics underneath the clouds of Jupiter. Nature Commun. 11 (1), 1–4.

Yadav, R.K., Bloxham, J., 2020. Deep rotating convection generates the polar hexagon on Saturn. Proc. Natl. Acad. Sci. http://dx.doi.org/10.1073/pnas.2000317117.

Yadav, R.K., Gastine, T., Christensen, U.R., Duarte, L., 2013. Consistent scaling laws in anelastic spherical shell dynamos. Astrophys. J. 774 (1), 6.

Yadav, R.K., Heimpel, M., Bloxham, J., 2020. Deep convection–driven vortex formation on Jupiter and Saturn. Sci. Adv. 6 (46), http://dx.doi.org/10.1126/sciadv.abb9298, eprint: Online. Available: https://advances.sciencemag.org/content/6/46/eabb9298.

Yano, J.-I., Talagr, O., Drossart, P., 2005. Deep two-dimensional turbulence: An idealized model for atmospheric jets of the giant outer planets. Geophys. Astrophys. Fluid Dyn. 99 (2), 137–150.